

Study on High-Speed Sensing and
High-Quality Image Reconstruction
for Photoacoustic Biomedical
Visualization Technology

(光超音波を用いた医用生体可視化技術に
おける高速センシングと高画質化に
関する研究)

丛 冰

CONTENTS

主論文 1

A Fast Acoustic Field Mapping Approach Based on Fabry-Perot Sensor with High-speed Camera

Bing Cong, Kengo Kondo, Makoto Yamakawa, Tsuyoshi Shiina, Takao Nakajima and Yasufumi Asao

IEEJ Trans. on Electr. Electron. Eng., Vol. 9, No. 5, pp. 477-483, 2014

DOI: 10.1002/tee. 21996

© 2014 Institute of Electrical Engineers of Japan. (<http://www.iee.jp>)

Published by John Wiley & Sons, Inc. (<http://onlinelibrary.wiley.com/>)

主論文 2

Photoacoustic image quality enhancement by estimating mean sound-speed based on optimum focsuing

Bing Cong, Kengo Kondo, Takeshi Namita, Makoto Yamakawa and Tsuyoshi Shiina

Jpn. J. Appl. Phys., Vol. 54, No. 7, 2015 (in press)

© 2015 The Japan Society of Applied Physics. (<http://www.jps.or.jp/>)

Published by IOP Publishing. (<http://iopscience.iop.org/>)

A Fast Acoustic Field Mapping Approach Based on Fabry–Perot Sensor with High-Speed Camera

Bing Cong^{*a}, Non-Member
Kengo Kondo^{*}, Non-Member
Makoto Yamakawa^{**}, Member
Tsuyoshi Shiina^{*}, Member
Takao Nakajima^{***}, Non-Member
Yasufumi Asao^{*,***}, Non-Member

A Fabry–Perot (FP) interferometer-based ultrasound sensor provides an inherently broadband response and excellent detection sensitivity compared to piezoelectric zirconate titanate (PZT) or polyvinylidene difluoride (PVDF) transducers. It is therefore expected to be used for medical ultrasound imaging and photoacoustic imaging. However, at present, mapping acoustic fields takes much time for scanning, which hinders real-time measurement. We propose a new approach that utilizes a high-speed camera (HSC) to map acoustic fields without mechanical scanning and to sample signals of acoustic waves with the shutter of the HSC. Experimental results indicate that acoustic field at the focus of a pulsed 1-MHz PZT ultrasound transducer can be detected and mapped by using the FP sensor with the HSC. By improving the uniformity of the FP sensor and the exposure time, the frame rate of HSC can be further developed, and this approach should be able to provide a fast acoustic field mapping for high-resolution biomedical photoacoustic and other ultrasonic imaging. © 2014 Institute of Electrical Engineers of Japan. Published by John Wiley & Sons, Inc.

Keywords: Fabry–Perot interferometer, high-speed camera, acoustic field mapping, photoacoustic imaging, ultrasonic imaging

Received 26 September 2012; Revised 10 April 2013

1. Introduction

Ultrasound imaging has significantly impacted clinical diagnosis in radiology, obstetrics, vascular examination, cardiology, emergency medicine, and intervention because of its real-time capabilities, non-ionizing properties, and much lower cost than any other medical modality [1]. It provides good penetration depth and image resolution but suffers from strong speckle artifacts as well as poor contrast in early stage tumors.

Photoacoustic imaging is a noninvasive imaging modality for visualizing the structure and function of soft tissues [2]. It has the potential to structurally image animal or human organs, such as the breast and the brain, with simultaneous high contrast and high spatial resolution [3]. Currently, most photoacoustic imaging instruments employ piezoelectric detectors to detect the photoacoustic signals. However, the sensitivity of piezoelectric detectors falls off with decreasing element size, thereby limiting the resolution of photoacoustic imaging.

A new imaging modality combining ultrasound imaging or photoacoustic imaging with optical ultrasound detection techniques may offer the potential to overcome this limitation [4]. This technique is based on the detection of acoustically induced changes in

the thickness of a planar Fabry–Perot (FP) polymer film interferometer. An ultrasound sensor based on the FP interferometer (FPI) can provide (i) broadband frequency responses of several tens of megahertz, (ii) optical element size of a few tens of micrometers, and (iii) excellent detection sensitivity of several hundreds of pascals comparable to those of broadband piezoelectric polyvinylidene difluoride (PVDF) detectors. It means that, by spatially sampling a relatively large aperture, a high-density ultrasound sensor array can be readily configured [5–10].

Mapping ultrasound fields in water for imaging purposes is most commonly achieved by two-dimensional (2D) mechanical scanning using a single piezoelectric detector. This includes optically scanning a focused laser beam over the surface of the sensor and detecting the reflected laser with a stationary photodiode [11], or illuminating the surface of the sensor with a large-diameter laser beam and mechanically scanning a photodiode over the reflected laser beam [12]. However, in the case of these systems, the data acquisition speed is unacceptably low. A rapid data acquisition approach consists of illuminating the sensor with a large-diameter laser beam and mapping the reflected laser beam in parallel at discrete time intervals using a 2D charge-coupled device (CCD) array. This concept is notionally similar to that of an acoustic camera taking snapshots of the acoustic field [13]. It samples signals of the acoustic field by switching the pulsed laser irradiation, which is not easy to realize at high-frequency sampling in the order of megahertz.

In this paper, we propose a new approach, in which we illuminate the sensor with a large-diameter continuous-wave (CW) laser beam and utilize a high-speed camera (HSC) to sample signals of the acoustic field with the shutter of HSC and to map the acoustic field without mechanical scanning. Experimental results indicate that the proposed method can sample signals of the order

^a Correspondence to: Bing Cong. E-mail: cb5515@gmail.com

^{*} Department of Human Health Science, Graduate School of Medicine, Kyoto University, 53 Kawahara-cho, Syogoin Sakyo-ku, Kyoto 606-8507, Japan

^{**} Advanced Biomedical Engineering Research Unit, Kyoto University, Yoshida-Honmachi, Sakyo-ku, Kyoto 606-8501, Japan

^{***} Canon Inc., 30-2 Shimomaruko 3-chome, Ohta-ku, Tokyo 146-8501, Japan

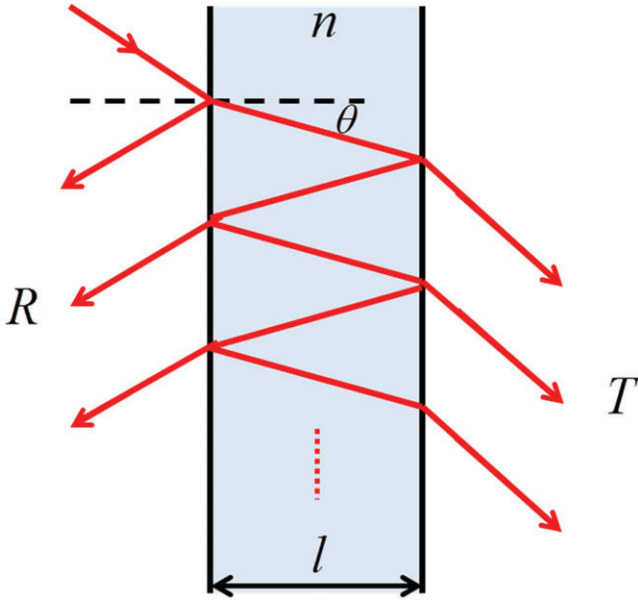


Fig. 1. Fabry–Perot interferometer (FPI). Light enters the FPI and undergoes multiple internal reflections

of megahertz and achieve faster data acquisition compared to conventional methods.

The rest of this paper is organized as follows. The acoustic signals detection principle of the FP ultrasound sensor and implementation of acoustic field mapping are given in Section 2. Section 3 describes the advantages of the proposed system. Section 4 describes the instrumental realization of the system and the results of the experiments. Finally, discussion and conclusions are given in Sections 5 and 6, respectively.

2. Method

2.1. Detection principle of the FP ultrasound sensor

An FPI is typically made of two parallel, highly reflecting mirrors. Figure 1 shows a schematic of the FP interferometer.

The phase between each succeeding reflection is given by Φ :

$$\Phi = \left(\frac{2\pi}{\lambda} \right) 2nl \cos \theta \quad (1)$$

where n is the refractive index of the material between the reflecting surfaces. If both surfaces have a reflectance R , the transmittance function of the FPI is given by

$$T = \frac{(1 - R)^2}{1 + R^2 - 2R \cos \delta} = \frac{1}{1 + F \sin^2(\Phi/2)} \quad (2)$$

where

$$F = \frac{4R}{(1 - R)^2} \quad (3)$$

is the coefficient of finesse [14].

From (2), we see that the interferometer transfer function (ITF) of the FPI is determined by the phase Φ caused by the multiple reflections of light between the two reflecting mirrors and by the reflectance R of the FPI, which is a constant factor and determined by the material of FPI. One of the ITFs of the FPI is shown in Fig. 2. If the phase Φ is in phase, then the ITF corresponds to a transmission maximum. If the phase Φ is out of phase, the ITF corresponds to a transmission minimum.

When an incident acoustic wave modulates the optical thickness l of the FPI, from (1), this modulation produces an optical phase difference $d\Phi$ and results in a corresponding reflected laser

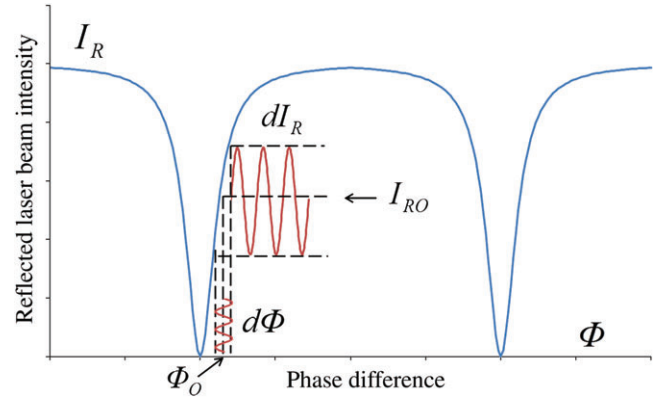


Fig. 2. Interferometer transfer function (ITF) showing the reflected laser intensity of the FPI as a function of the phase Φ . The diagram illustrates that at the optimum phase Φ_0 FPI has a maximum detection dI_R , acoustically induced by phase the difference $d\Phi$

intensity change dI_R . Then the incident acoustic pressure can be linearly approximated as the change of the reflected laser intensity, which means the incident acoustic wave can be detected by the FPI as a change in the reflected laser intensity.

From Fig. 2, it is clear that, when Φ corresponds to the point of maximum slope of the ITF curve, the phase difference $d\Phi$ can result in a maximum in the reflected laser intensity change dI_R , which means that the FPI has maximum detection sensitivity. Additionally, from (2), we also see that the FPI with a higher finesse F results in a sharper ITF curve and the same phase difference can result in a larger reflected laser intensity change, which means the detection sensitivity of the FPI also depends on the finesse F .

A schematic of our FP ultrasound sensor is shown in Fig. 3. It comprises a glass backing stub onto which a 30- μm -thick polymer (Parylene C) film spacer sandwiched between the dielectric multilayer mirrors is deposited in order to form the FPI. An antireflective (AR) coating is deposited onto the glass backing stub to reduce the laser reflection from its top surface. For the same reason, the glass backing stub is wedged to eliminate the interference between light reflected from its upper surface and the FPI. Finally, a thin polymer film is deposited over the entire structure to protect the external FPI sensor from damage due to abrasion or water ingress.

Because the thickness of FPI is up to several tens of micrometers, it is difficult to keep uniformity of the thickness of the FPI. So, we must point out that, from (1) and (2), the ITF corresponding to each FP sensor element is not the same because of the

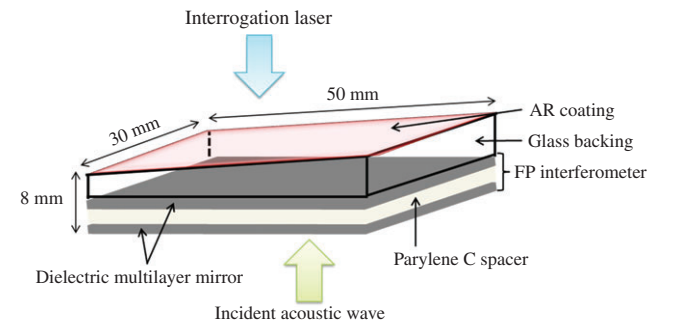


Fig. 3. FP ultrasound sensor. A Parylene C film spacer sandwiched between the two dielectric multilayer mirrors forms the FPI. The glass backing stub is wedged to eliminate the interference between light reflected from its upper surface and the FPI

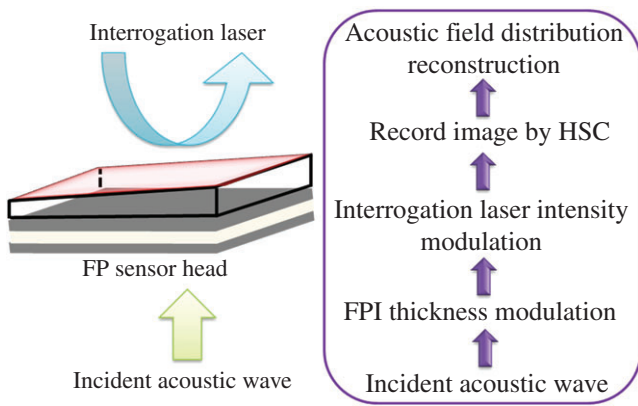


Fig. 4. Detecting principle of the FP sensor. The incident acoustic pressure can be linearly approximated as the change of reflected laser intensity, and the image of the reflected laser intensity corresponding to the optimum wavelength of all sensor points can be considered as the acoustic field distribution

variation in the thickness of the FPI. An FP sensor tuning process to find the optimum wavelength of the incident laser for the maximum FPI detection sensitivity needs to be done for each FP sensor point. This tuning process and one of the ITFs of our FP sensor are described in Section 2.2.

The detection principle of acoustic wave signals by the FP ultrasound sensor can be summarized as in Fig. 4. An interrogation laser illuminates the sensor over the surface, and the reflected laser beam is imaged onto the complementary metal-oxide-semiconductor (CMOS) area sensor of the HSC. In the absence of an incident acoustic wave, the reflected laser intensity remains the same. When an acoustic wave is injected into the FP sensor, the incident acoustic wave modulates the thickness of the FPI. This modulation produces an optical phase difference and results in a corresponding modulation of the reflected laser intensity. After recording the images of the reflected laser intensity, one can reconstruct the acoustic field distribution by using the reflected laser intensity data corresponding to the optimum wavelength for each sensor point.

We use the shutter of the HSC to sample the reflected laser intensity signals, but the frame rate of the HSC is not high enough to sample megahertz signals even if the maximum frame rate is up to 1.5 MHz. We broke this limitation by sampling signals at different time delays after the excitation of the acoustic wave by sacrificing some data acquisition speed. Additionally, the interrogation laser illuminates the FP sensor perpendicularly always, and so no change of the reflected laser intensity induced by the change of incident angle is imaged onto the HSC. In other words, only the change of reflected laser intensity induced by the incident acoustic wave is imaged onto the HSC.

2.2. FP ultrasound sensor tuning Because of the variation in the thickness of the FPI, for obtaining maximum sensor detection sensitivity for each FP sensor element it is necessary to find the optimum wavelength of the interrogation laser so that it corresponds to the point of maximum slope on the ITF curve. We call this process *sensor tuning* or *bias*. The sensor tuning process must be performed for each sensor element. For each sensor element biased, the FP sensor can be said to be optimally biased. When the sensor is optimally biased, the signal of the incident acoustic wave can, in principle, be obtained as a change in the interrogation laser intensity.

The procedure for obtaining the ITF curves for all FP sensor elements is described as follows: In the absence of an incident acoustic wave, a 5-mm-diameter laser beam illuminates the sensor

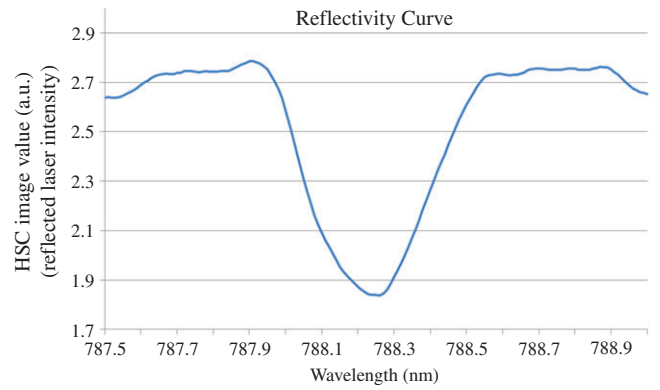


Fig. 5. ITF curve for one FP sensor element. If, at the wavelength corresponding to the point of maximum slope on the curve, the reflected optical intensity modulation due to an acoustically induced phase difference is a maximum value, then this sensor element can be said to be optimally biased

and the beam reflected from the sensor is imaged onto a CMOS area sensor. From this HSC image, we can obtain the HSC image value corresponding to a fixed interrogation laser wavelength for each sensor element. Then the interrogation laser wavelength is swept from 787.5 to 789 nm in steps of 15 pm, and 100 HSC images are recorded. From those 100 images, the ITF of each sensor point can be obtained as a function of the laser wavelength by plotting the HSC image values corresponding to all 100 wavelengths for each sensor element. One of the ITFs of our FP sensor is shown in Fig. 5. Then, after a moving-average process of those ITF curves, we can find the optimum wavelengths by differentiating the reflectivity curves.

2.3. Acoustic field mapping implementation

The acoustic field mapping implementation is composed of two processes: the FP sensor tuning process and the acoustic wave signal acquisition process. The flowchart and timing chart of these processes are presented in Figs 6 and 7, respectively and the procedure is described below in detail.

After the sensor tuning process described in Section 2.2, the lateral spatial distribution of the incident acoustic field is mapped onto the optical beam reflected from the sensor and can be spatially resolved by using the HSC. The HSC snapshots of the incident acoustic field distribution can be recorded at all discrete time delays after the excitation of acoustic wave and all

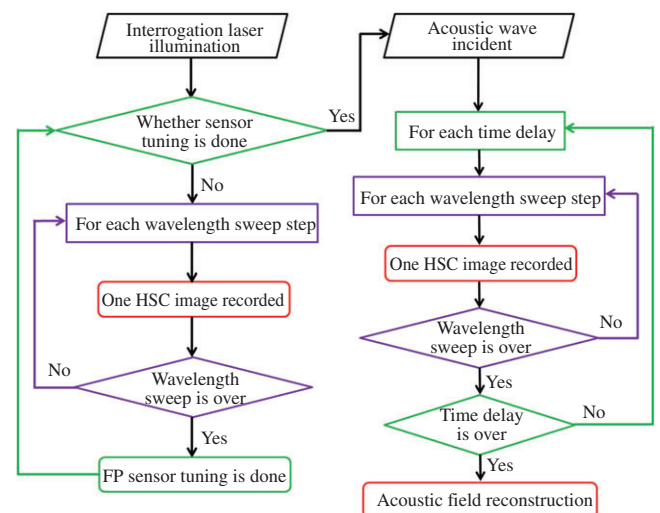


Fig. 6. Flowchart of the acoustic field mapping procedure

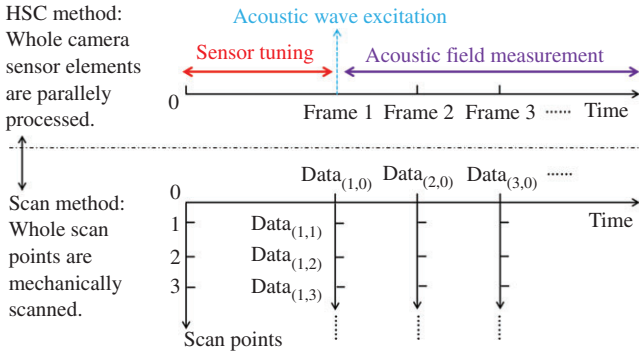


Fig. 7. Timing chart of sensor tuning and the acoustic field measurement. The whole scan points are processed in parallel in the proposed HSC method

swept wavelength steps. Then the acoustic wave signal acquisition process is finished. For all camera elements, the image value data for the optimum wavelengths, which correspond to the elements at a discrete time, are used to reconstruct the acoustic field distribution of this discrete time. It should be noticed that the incident acoustic wave results in a corresponding change in the reflected interrogation laser intensity while the HSC images correspond to the reflected laser intensity. Briefly, the HSC image value data with the removed DC component are used to reconstruct the acoustic field distributions.

Sensor tuning needs to be done both for the conventional method and the proposed method. But as shown in Fig. 7, in the proposed HSC method both sensor tuning and acoustic field measurement can be done in parallel for the whole HSC sensor elements without mechanical scanning, so the total experimental time is far shorter than for the conventional scan method. Additionally, from Fig. 5 it is possible that the pressure of the incident acoustic wave is large enough, and so the change of the reflected laser intensity induced by that will exceed the detection limit, which can violate the linear approximation of the FPI detecting principle. We will discuss these topics in detail while showing the experimental data in Section 5.

3. System Advantages

The difference in the system between the conventional scan method and the proposed HSC method is shown in Fig. 8. The HSC method has two main advantages over the scan method.

First, the sensor tuning time and the data acquisition time are improved. In the scan method, sensor tuning and data acquisition should be done as the focusing laser mechanically scans the sensor. Assuming that scan area size is $m \times n$, the wavelength sweep time

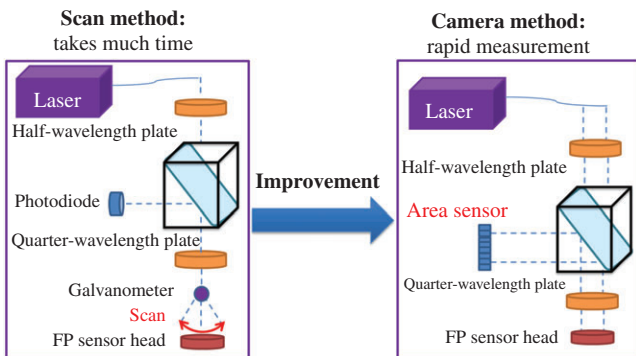


Fig. 8. System difference between the conventional scan method and the proposed HSC method

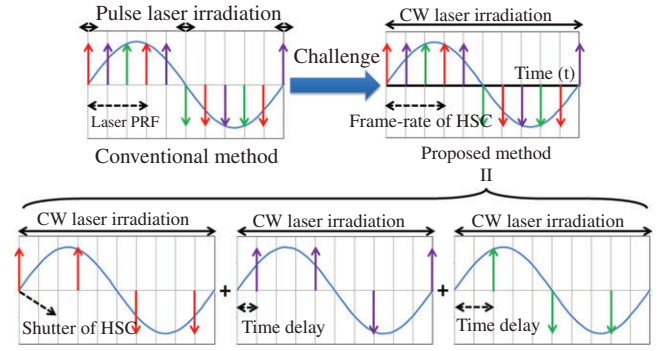


Fig. 9. Difference of signal sampling method between the conventional scan method and the proposed HSC method

is τ_{sp} , the scan time to the next scan point is τ_{sc} , and the optimum wavelength setting time is τ_b , the sensor tuning time T'_b and the data acquisition time T'_a are, respectively, given as follows:

$$T'_b = m \times n \times (\tau_{sp} + \tau_{sc}) \quad (4)$$

$$T'_a = m \times n \times (\tau_b + \tau_{sc}) \quad (5)$$

Then the total experimental time is T' given by

$$T' = T'_b + T'_a = m \times n \times (\tau_{sp} + 2\tau_{sc} + \tau_b) \quad (6)$$

In the HSC method, the sensor tuning time T_b and the data acquisition time T_a are, respectively, given by

$$T_b = \tau_{sp} \quad (7)$$

$$T_a = \tau_{sp} \quad (8)$$

and the total experiment time T is given by

$$T = T_b + T_a = 2\tau_{sp} \quad (9)$$

As a result, the ratio of the times between the conventional scan method and the proposed HSC method is represented by

$$T'/T = m \times n \times (\tau_{sp} + 2\tau_{sc} + \tau_b)/2\tau_{sp} \approx m \times n/2 \quad (10)$$

$$T'_a/T_a = m \times n \times (\tau_b + \tau_{sc})/\tau_{sp} \quad (11)$$

From (10) and (11), it is obvious that total experiment time and data acquisition time are further improved when the scan area increases. In our experimental condition, the measurement area ($m \times n$) is 128×128 elements, the wavelength sweep time (τ_{sp}) is 11 979 s, and the sum of τ_{sc} and τ_b of the scan method is 1 s, so the total experiment time and data acquisition time are improved by 8193 times and 1.3 times, respectively.

Second, from the difference in the laser switching method between the scan method and the HSC method, as shown in Fig. 9, the HSC method can detect higher frequency acoustic signals because the frame rate of HSC is significantly higher than the pulse repetition frequency (PRF) of the pulsed laser. However, in the current stage, the frame rate of the HSC is not high enough to sample tens of megahertz signals even though the maximum frame rate can go up to 1.5 MHz. Therefore, we sample the signals at different time delays after the excitation of the acoustic wave with the frame rate of the HSC, and then combine those discrete data by using a post-processing program.

4. Experiments

4.1. System Setup The practical implementation of the FP sensor and the HSC-based acoustic field mapping system is shown in Fig. 10.

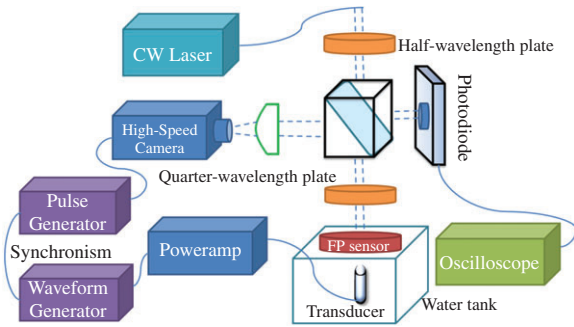


Fig. 10. FPI-based acoustic field mapping system

A 5-mm-diameter laser beam from TLS (TL780-B, Thorlabs Inc., Newton, New Jersey, USA) illuminates the sensor, and the beam reflected from the sensor is imaged onto an HSC (Phantom V710, Vision Research Inc., Wayne, New Jersey, USA) with the CMOS area sensor of 128×128 elements ($2.56 \times 2.56 \text{ mm}^2$). The interrogation laser wavelength is swept at intervals of 15 pm from 787.5 to 789 nm. From Fig. 5, the swept wavelength size should be less than the width of the ITF curve and a smaller size leads to higher detecting sensitivity and longer experiment time, so we select 30 pm considering the balance between the experimental time and detection sensitivity.

The sensor is mounted on the top of a full water tank, and a focused 1-MHz piezoelectric zirconate titanate (PZT) transducer (v314-su, OLYMPUS Inc., Shinjuku-ku, Tokyo, Japan) is placed near the focal length of 25.4 mm. The transducer is driven by a waveform generator and a power amplifier at a repetition rate of 1 kHz. The pulse generator is triggered by the waveform generator, and a discrete delay time Δt is introduced in order to synchronize the timing of HSC shutter after the emission of the acoustic wave, which means sampling the signal of the acoustic wave by the shutter of the HSC. The total delay time T should be longer than the width of incident acoustic wave signal pulse and can be calculated from $N \times \Delta t$, where N is a natural number and up to 40 for our experiment. Δt and N can be determined by the achieved virtual sampling frequency and the acquired acoustic wave signal length, respectively.

In our experiment, Δt is 125 ns and the achieved virtual sampling frequency is 8 MHz, which is sufficient to sample 1-MHz incident acoustic wave signals. But we must also point out that the minimum exposure time of the HSC is 294 ns, which is longer than the delay time Δt , which means that the reflected laser intensity curve is smoothed and the detecting sensitivity reduced. The peak intensity of the incident acoustic pulse is 13 kPa, which is within the linear operating range of the FP sensor and close to the intensity of the photoacoustic signals generated in tissues, which are the detecting target of the proposed method, in the order of kilopascals. Therefore, the acoustic field distribution near the focus can be detected by the FP sensor. Then the acoustic field distribution detected by FP sensor can be sampled and recorded by the HSC. By using this system setup, we can verify the usefulness of the proposed method. The interrogation laser beam is also incident on a single photodiode, and the output of photodiode is recorded by a digitizing oscilloscope to cut off the change in output of the laser that is not induced by the incident acoustic wave. All data of the camera and oscilloscope are downloaded to a note personal computer (CF-S8, Panasonic Inc., Kadoma-shi, Osaka, Japan) via a local area network (LAN). Then, we can reconstruct the acoustic field distribution from the HSC images and the optimum wavelength distribution of the FP sensor.

4.2. Experimental Results One HSC image of the output of the FP sensor at the laser wavelength of 788.18 nm is

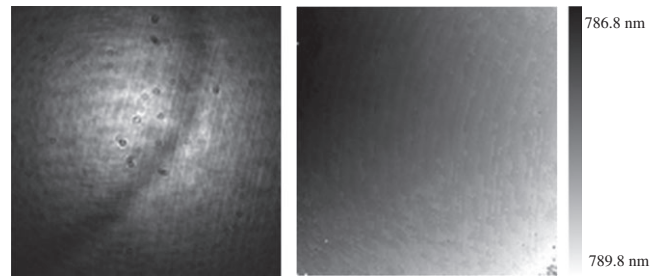


Fig. 11. One HSC image of the output of the FP sensor (left) and the optimum wavelength distribution of the FP sensor (right)

shown in Fig. 11(left). From Fig. 2, we know that the reflected laser intensity changes as a result of the change both in the laser wavelength and the FPI thickness. When the laser wavelength is fixed, because of the variation in thickness of the FPI, the arc-shaped location, which is darker than the surrounding area, can be visually observed. In other words, the current wavelength is the optimum wavelength for the arc-shaped location. According to a previous study, the FPI shows concentric elliptical transmission fringes under narrowband visible illumination. Figure 11(left) shows an arc-shaped fringe because of the fixed interrogation laser wavelength, and only a part of the whole FP sensor is shown.

The optimum wavelength distribution of the FP sensor can be reconstructed by calculating the optimum wavelength for each sensor element from the HSC images of all swept laser wavelengths. The optimum wavelength distribution of the FP sensor is shown in Fig. 11(right). It shows the optimum wavelength increase from the upper left to the lower right. Because of the instability of laser output power and the Gaussian beam profile of the laser, it is difficult to accurately calculate the optimum wavelengths of the FP sensor, which also may impair the detection sensitivity of our system.

Figure 12 shows that the signal detected by the FP sensor is in agreement with that detected by the hydrophone previously. The corresponding acoustic field distributions induced by the transducer at the positive peak (A: $t = 20.125 \mu\text{s}$) and negative peak (B: $t = 19.625 \mu\text{s}$) are depicted in Fig. 13 (left) and (right), respectively. The reconstructed acoustic field distribution appears as a circular region of uniform amplitude, which is characteristic of the planar nature of the wavefront at the focus of the acoustic field. The diameter of this region is approximately 5 mm.

Additionally, Fig. 12 shows that the noise of the signal detected by the FP sensor is more than that detected by the hydrophone. Several reasons can be considered. First, the noise in the area sensor of the HSC may reduce the sensor detection sensitivity. From Fig. 11 (left), it can be seen that the sensitivity of the camera sensor is not high enough; even some sensor elements are broken.

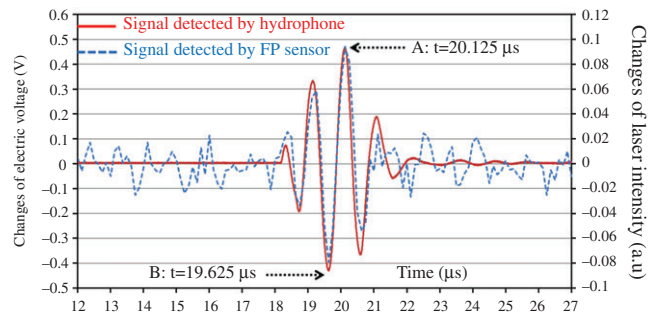


Fig. 12. Signal waves detected by the hydrophone and the FP sensor. The output of hydrophone means the changes of electric voltage, and the international unit is volts. The output of the FP sensor means the changes of reflected laser beam intensity and the unit is arbitrary

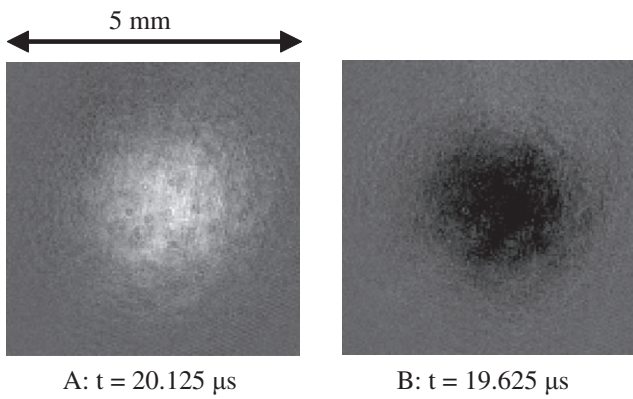


Fig. 13. Reconstructed acoustic field distribution at positive peak (left) and negative peak (right) of the signal of the acoustic wave detected by the FP sensor. In order to obtain a good contrast, the dynamic range has been narrowed

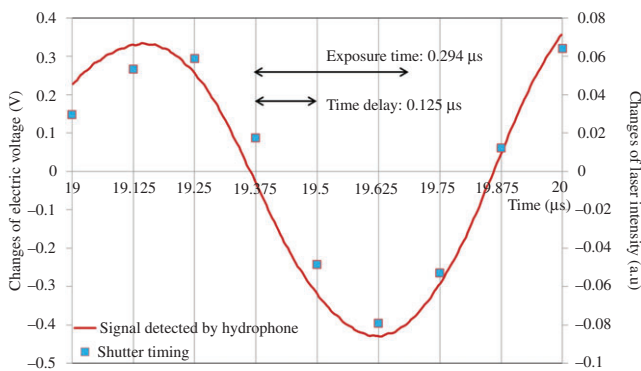


Fig. 14. Relationship between the signal wave detected by the FP sensor and the shutter timing

Second, the output power of laser is not stable. Variations of the laser output power leads to changes in the reflected laser intensity that are not induced by the incident acoustic wave. Finally, the large swept wavelength size may also reduce the sensor detection sensitivity. Meanwhile, there is a tradeoff between the swept wavelength size and the sensor detection sensitivity.

Figure 14 shows a close-up of Fig. 10 from 19 to 20 μs . From Fig. 14, we can readily see that the shutter timing interval is 125 ns, so the achieved sampling frequency is obviously 8 MHz. We can also reconfirm that the signal wave detected by the FP sensor and the HSC is in agreement with that detected by the hydrophone previously. We must point out that the exposure time of the HSC is 294 ns, which is the minimum settable value of the camera but also 2.5 times longer than the shutter sampling time, and that leads to decreased FP sensor detection sensitivity.

In our HSC method, we illuminate the FP sensor with large-diameter CW laser beam and utilize the HSC to sample signals of acoustic waves without mechanical scanning, so the data acquisition time is shorter than that with the scanning method. In practice, we failed to synchronize the camera and laser because TL780-B is a prototype laser. Therefore, we were obliged to sweep the laser wavelength discretely but not continuously, which significantly reduced the sensor tuning speed and the data acquisition speed. We will discuss this in detail in next section.

5. Discussion

We would like to point out that the sensor tuning process needs to be carried out only once. When the FP sensor is

optimally biased, it is not necessary to tune the sensor for data acquisition each time. Furthermore, the temporal resolution of our HSC method is determined by the laser wavelength sweep time because the signal processing time is significantly less than the wavelength sweep time. Because TL780-B is a prototype laser, we were obliged to sweep the laser wavelength discretely. Lesser laser sweep time, which can be achieved by sweeping the laser continuously, can provide further improvement in the data acquisition time.

If the pressure of the incident acoustic wave is large enough, then the change of the reflected laser intensity induced by that may exceed the linear approximation of the FPI detecting principle. In our experiment, from Fig. 11, we can see that the change of laser intensity induced by the incident acoustic wave is around 0.16. That is 6 times smaller than the change of the laser intensity of the FPI, as shown in Fig. 5, which is around 1. However, for our 30- μm FPI, the upper limit of linear detection is above 1.5 MPa. In general, the peak intensity of photoacoustic signals generated in tissues is of the order of kilopascals and therefore within the linear range [4]. Normally, a number of incident acoustic waves that have different frequencies and amplitudes should be used to verify the usefulness of the proposed method, but only a 1-MHz acoustic wave signal with a peak value of 13 kPa was used in this paper because of the limitations of the HSC frame rate and the discrete sweep of the laser.

There are some limitations that may impair the performance of our system. First, the lower power of the interrogator laser due to spreading of the laser beam to illuminate the whole sensor may smooth the wavelength-dependent reflectivity curve which is used to calculate the optimum wavelength distribution. Additionally, the long exposure time of the HSC also smooths the changes of laser output intensity which would lead to a reduction of the sensor detection sensitivity. Second, the optimum wavelength of the sensor is not one in practice, owing to the variations in the optical thickness of the sensor. The number of the optimum wavelengths of the sensor may significantly increase the data acquisition time. But the variation in the optical thickness of the sensor can be neglected over the relatively small area of the sensor [13].

6. Conclusion

In this paper, a new method of acoustic field mapping based upon an FP ultrasound sensor and HSC has been successfully demonstrated by imaging the acoustic field at the focus of a pulsed 1-MHz PZT transducer. The concept is similar to that of an acoustic camera taking snapshots of acoustic field distributions as used to map the output of other optical ultrasound sensors [15,16]. This approach is the first attempt to detect an acoustic wave signal with a CW laser and sample the acoustic wave signal with the shutter of the HSC. The improvement in frequency of the signal that can be detected is an encouraging step toward fast photoacoustic signal detection and imaging. The proposed method also has the potential to become a fast acoustic field mapping method for high-resolution biomedical photoacoustic imaging and other ultrasonic imaging modalities even though at present the time of acoustic field mapping, which is in the range of tens of minutes, is still not sufficient.

Acknowledgments

This work was sponsored by the Health and Labour Sciences Research Grants, Ministry of Health, Labour and Welfare (MHLW), Japan, from 2009 to 2012 and partly supported by the Innovative Techno-Hub for integrated Medical Bio-imaging Project of the Special Coordination Funds for Promoting Science and Technology, Ministry of Education, Culture, Sport, Science and Technology (MEXT), Japan.

References

- (1) Minin IV, Minin OV. *Ultrasound Imaging—Medical Applications*. InTech: New York; 2011.
- (2) Wang X, Pang Y, Ku G, Xie X, Stoica G, Wang LV. Noninvasive laser-induced photoacoustic tomography for structural and functional in vivo imaging of the brain. *Nature Biotechnology* 2003; **21**(7):803–806.
- (3) Xu M, Wang LV. Photoacoustic imaging in biomedicine. *Review of Scientific Instruments* 2006; **77**:041101-(1–22).
- (4) Zhang E, Laufer J, Beard P. Backward-mode multiwavelength photoacoustic scanner using a planar Fabry-Perot polymer film ultrasound sensor for high-resolution three-dimensional imaging of biological tissues. *Applied Optics* 2008; **47**(4):561–577.
- (5) Kostli KP, Frenz M, Weber HP, Paltauf G, Schmidt-Kloiber H. Photoacoustic tomography: time-gated measurement of pressure distributions and image reconstruction. *Applied Optics* 2001; **40**(22):3800–3809.
- (6) Hamilton JD, O'Donnell M. High frequency ultrasound imaging with optical arrays. *IEEE Transactions on Ultrasonics, Ferroelectrics, and Frequency Control* 1998; **45**(1):216–235.
- (7) Beard PC, Perennes F, Mills TN. Transduction mechanisms of the Fabry-Perot polymer film sensing concept for wideband ultrasound detection. *IEEE Transactions on Ultrasonics, Ferroelectrics, and Frequency Control* 1999; **46**(6):1575–1582.
- (8) Uno Y, Nakamura K. Pressure sensitivity of a fiber-optic microprobe for high-frequency ultrasonic field. *Japanese Journal of Applied Physics* 1999; **38**:3120–3123.
- (9) Askenazi S, Witte R, O'Donnell M. High frequency ultrasound imaging using a Fabry-Perot etalon. *Proceedings of SPIE* 2005; **5697**:243–250.
- (10) Zhang EZ, Beard P. Ultra high sensitivity, wideband Fabry-Perot ultrasound sensors as an alternative to piezoelectric PVDF transducers for biomedical photoacoustic detection. *Proceedings of SPIE* 2004; **5320**:222–229.
- (11) Cox BT, Zhang EZ, Laufer JG, Beard PC. Fabry-Perot polymer film fibre-optic hydrophones and arrays for ultrasound field characterization. *J. Phys.: Conf. Ser.* 2004; **1**:32–37.
- (12) Beard PC. 2D ultrasound receive array using an angle-tuned Fabry Perot polymer film sensor for transducer field characterization and transmission ultrasound imaging. *IEEE Transactions on Ultrasonics, Ferroelectrics, and Frequency Control* 2005; **52**(6):1002–1012.
- (13) Lamont M, Beard PC. 2D imaging of ultrasound fields using CCD array to map output of Fabry-Perot polymer film sensor. *Electronics Letters* 2006; **42**(3):187–189.
- (14) Hernandez G. *Fabry-Perot Interferometers*. Cambridge University Press: Cambridge; 1986.
- (15) Klann M, Koch C. Measurement of spatial cross sections of ultrasound pressure fields by optical scanning means. *IEEE Transactions on Ultrasonics, Ferroelectrics, and Frequency Control* 2005; **52**(9):1546–1554.
- (16) Paltauf G, Schmidt-Kloiber H. Optical method for two dimensional ultrasonic detection. *Applied Physics Letter* 1999; **75**(8):1048–1050.

Bing Cong (Non-member) received the B.S. degree in computer science from University of Tsukuba, Ibaraki, Japan, in 2009, and the M.S. degree in Human Health Science from Kyoto University (KU), Kyoto, Japan, in 2011. He is currently working toward the Ph.D. degree in the Department of Human Health Science, KU. His research interests include Fabry-Perot ultrasound sensors, photoacoustic microscopes, and photoacoustic image reconstruction.



Kengo Kondo (Non-member) graduated from the College of Information Sciences, University of Tsukuba (UT), Japan, in 2005. He received the M.E. and Ph.D. degrees in Engineering in 2007 and 2010, respectively, from UT. He is presently a Program-specific researcher with Kyoto University. His research interests include tissue characterization, especially using ultrasonic elasticity imaging and photoacoustic imaging. Dr. Kondo is a member of the Japan Society of Ultrasonics in Medicine.



Makoto Yamakawa (member) received the M.E. and Ph.D. degrees from the University of Tsukuba, Japan, in 1999 and 2002, respectively. He is presently an Associate Professor with Kyoto University. He has worked on tissue characterization using ultrasound. Dr. Yamakawa is a member of the Japan Society of Ultrasonics in Medicine and The Institute of Electronics, Information and Communication Engineers.



Tsuyoshi Shiina (member) graduated from the Electronic Engineering Department, University of Tokyo (UT), in 1982. He received the M.S. and Ph.D. degrees in Electronic Engineering in 1984 and 1987, respectively, from UT. He also received the Doctor of Medical Science degree in 2006, from the University of Tsukuba. In 2001, he became a Professor with the Graduate School of Systems and Information Engineering, University of Tsukuba. He is presently a Professor with the Graduate School of Medicine, Kyoto University. His current research interests include visualization technique of structural and functional bioinformation, for example, ultrasonic elasticity imaging and photoacoustic imaging. He was awarded the Prize for Science and Technology for the Ultrasound Tissue Elasticity Imaging System by MEXT 2010. Prof. Shiina has worked as chairperson of the technological committee of Medical Engineering in IEEE. He is councilor of the Japan Society of Medical Electronics and Biological Engineering. He is also an Executive Trustee of the Japan Society of Ultrasonics in Medicine (JSUM).



Takao Nakajima (Non-member) graduated from the Department of Applied Physics, University of Tokyo, Tokyo, in 2004, and received the M.S. degree in Physical Engineering in 2006. He has been working with Canon Inc. since 2006. His research interests include the development of photoacoustic microscope and the Fabry-Perot ultrasound sensor as well as clinical studies using photoacoustic tomography for breast cancer diagnosis.



Yasufumi Asao (Non-member) received the B.S., M.S., and Ph.D. degrees in Electronic Engineering from Tohoku University, Miyagi, Japan, in 1991, 1993, and 2005, respectively. He has been working with Canon Inc. since 1993. He has been concurrently working as an Associate Professor with the Graduate School of Medicine, Kyoto University, since 2010. His research interests include the development of the Fabry-Perot ultrasound sensor and photoacoustic microscope as well as the clinical study using photoacoustic tomography for breast cancer diagnosis.



Photoacoustic image quality enhancement by estimating mean sound speed based on optimum focusing

Bing Cong^{1*}, Kengo Kondo², Takeshi Namita¹, Makoto Yamakawa³, and Tsuyoshi Shiina¹

¹*Department of Human Health Sciences, Graduate School of Medicine, Kyoto University, Kyoto 606-8507, Japan*

²*Integrated Medical System Unit for Fruitful Healthy-Longevity Society, Kyoto University, Kyoto 606-8507, Japan*

³*Advanced Biomedical Engineering Research Unit, Kyoto University, Kyoto 606-8507, Japan*

E-mail: cb5515@gmail.com

A constant sound speed (i.e., 1540 m/s) is generally used in various ultrasound (US) and photoacoustic (PA) image reconstruction algorithms based on the assumption of a homogeneous sound speed in human tissue. However, the variation of the sound speed in human tissue can be as great as 10%, which can lead to low contrast, distortion, and blurring in reconstruction images. We proposed an automatic method of selecting the mean sound speed based on optimum focusing of received PA signals to enhance the quality of reconstructed PA images. Optimum focusing is quantified by calculating the minimum sum of the deviation of beamformed PA signals from their mean value for various sound speeds. The proposed method was demonstrated by homogeneous and heterogeneous sound speed simulation models, and also evaluated by experiments with agar and porcine tissue-mimicking phantoms. The central vertical and lateral profiles of reconstructed absorbers verified the improvement of contrast, signal-to-noise ratio (SNR), and spatial resolution by using the estimated mean sound speed.

1. Introduction

Photoacoustic imaging (PAI) in biomedical applications is a noninvasive imaging modality and has been studied actively and widely in the last few decades.¹⁾ The photoacoustic (PA) effect refers to the generation of acoustic waves by the absorption of optical energy due to thermoelastic expansion.²⁾ The generated acoustic waves can then be detected on the surface of a body by ultrasound (US) transducers and be used to reconstruct a PA image, which is the distribution of optical energy absorption. From the difference in absorbed optical energy between human organs and tumors with a laser of a suitable wavelength, PAI has the potential to visualize structural information, such as tumors, cancers, and blood vessels.³⁻⁴⁾ Also because deoxyhemoglobin (HbR) and oxyhemoglobin (HbO₂) are two major optical absorbers, and the molar extinction between them is different, PAI has the potential to visualize functional information, such as hemoglobin oxygen saturation (SO₂), for understanding brain hemodynamics.⁵⁻⁶⁾ In addition, PAI has the advantages of high contrast of optical imaging and high spatial resolution of ultrasound imaging, both of which are important in diagnosing diseases.^{4,7)} PAI based on a high-sensitivity and wideband Fabry-Perot polymer film interferometer, which has been used as an alternative to a piezoelectric transducer, can provide faster and higher resolution PA and US imaging.⁸⁻⁹⁾ Various optical- and ultrasound-based imaging techniques can also be combined with PAI to provide the structural, functional, and biomechanical properties of human tissue.¹⁰⁻¹²⁾

The simplest reconstruction algorithm is the delay and sum (DAS) algorithm, which is a beamforming technique used in US imaging.¹³⁾ The most popular reconstruction algorithm is universal back-projection (UBP), which is based on the analytical solution of the wave equation.¹⁴⁻¹⁶⁾ When the detection surface is a closed spherical or open planar surface and the sound speed is homogeneous, UBP can quantitatively reconstruct the initial optical absorption. Indeed, when human tissue is heterogeneous, UBP is also an "approximate" reconstruction method. The least restrictive reconstruction algorithm is time reversal (TR), which is guaranteed in odd dimensions and an acoustically homogeneous medium, and is approximately true in even dimensions and an acoustically heterogeneous medium.¹⁷⁻¹⁸⁾ The detection surface in TR algorithm can be any closed shape and the image at any time can be reconstructed. Actually, closed spherical scanning and infinite planar scanning are generally difficult to implement in a clinical application. To overcome this limited-view problem, various iterative reconstruction algorithms (also called model-based reconstruction algorithms) have been proposed.¹⁹⁻²¹⁾ In these methods, the inverse problem is converted into solving an optimization problem by minimizing the error between

detected PA signals and calculated PA signals from the initial absorbed optical energy by a forward acoustic wave propagation model. The iterative reconstruction algorithms require more memory and computational complexity but provide higher accuracy and can model nonideal measurement environments. When looking for the "best" reconstruction algorithm to use in practice or research, we should comprehensively consider the accuracy, speed, generality, computational cost, system requirements, and so forth.²²⁻²³⁾

Sound speeds in human tissue can vary by as much as 10%, between 1400 and 1450 m/s for subcutaneous fat and between 1500 and 1560 m/s for normal parenchyma and stromal tissue. In general, sound speed errors have a significant impact on the spatial resolution and amplitude sensitivity of reconstructed PA and US images.²⁴⁻²⁵⁾ Wang's group proposed a compensation method using the sound speed distribution obtained from ultrasonic transmission tomography (UTT) to improve the contrast, distortion, and blurring of reconstructed PA images, but this method requires complicated experimental equipment, substantial amounts of numerical computation, and a closed-circle geometric structure for detection around optical absorbers in two dimensions (2D), which is usually unrealistic in clinical examination.²⁶⁾ As a low-cost alternative sound speed compensation method, an optimum sound speed estimated by maximizing the sharpness of the reconstructed image, as quantified by a focus quality function to provide the best image quality, has been proposed by Beard's group.²⁷⁾ However, this method requires strong absorbers or sharp edge boundaries, which are also unusual in human tissue. In medical US imaging, a constant sound speed (i.e., 1540 m/s) is also generally used for delay and focusing, which leads to defocusing due to variations of the sound speed in human tissue. To improve the B-mode image quality, a mean sound speed that provides the optimum focusing by minimizing the average phase variance or maximizing the mean spectral energy of beamformed radio-frequency (RF) data with different sound speeds has also been proposed.²⁸⁻²⁹⁾ In this paper, we propose a mean sound speed that can optimally focus received PA signals. The focus quality function is quantified by calculating the minimum average sum of the difference between beamformed PA signals and their mean value for various sound speeds, which is similar to the method used in US imaging. Note that because the laser irradiation cannot be focused as in transmission focusing in US imaging, similar conventional methods used in PA imaging are not applicable to large-diameter absorbers. We first choose a sufficiently large region of interest (ROI) for the absorber and calculate the focus quality value for each scanline. Then the scanline providing the minimum value is considered as the center position of the absorber. Next, we recalculate the focus quality

value of the estimated scanline for each sound speed, and the sound speed providing the minimum value can be estimated as the optimum mean sound speed of the area between the ROI and the sensor array. Finally, the estimated sound speed is then used to enhance reconstructed PA images. We verified the proposed mean sound speed estimation method using homogeneous and heterogeneous models for the sound speed with pointlike and large-diameter absorbers placed at different depths and sensor positions. We also evaluated its performance by calculating the full width at half maximum (FWHM) of lateral and vertical profiles of reconstructed absorbers and the signal-to-noise ratio (SNR) of reconstructed PA images.

The rest of this paper is organized as follows. Section 2 presents the principle and the implementation of mean sound speed estimation. Numerical simulations and phantom experiments are described in Sects. 3 and 4, respectively. Finally, we discuss and conclude our study in Sects. 5 and 6, respectively.

2. Method

2.1 PA signal beamforming

Figure 1(a) depicts detected PA signals generated from a pointlike absorber by a 32-channel linear sensor array as shown in Fig. 1(b).³⁰⁾ To focus the detected PA signals at a focal point (x, z) , the focusing delay time for the n th element (x_n, z_n) can be calculated by

$$d_n = (\sqrt{(x - x_n)^2 + (z - z_n)^2} - F) / c, \quad (1)$$

where F is the focal point depth and c is the real sound speed.

As shown in Eq. (1), the focusing delay time d_n is a function of the sound speed. When calculating the focusing delay times for all sensor elements, if the sound speed used to calculate the focusing delay time d_n is equal to the real sound speed c , the beamformed PA signals are in phase [Fig. 2(a)], and the intensity of the summed beamformed signals can be coherently enhanced [Fig. 2(b)]. Otherwise, if the sound speed is incorrect, phase distortion is introduced, which leads to decreased intensity of the summed beamformed signals [Fig. 2(c)]. Therefore, the average sum of the deviation of the focused PA signals from their mean value can be a minimum and lower than that of defocused PA signals. This theory can be used to optimally focus detected PA signals, and the sound speed providing the minimum value can be estimated as the optimum mean sound speed.

2.2 Mean sound speed estimation

The focus quality function Q , which is utilized to evaluate whether PA signals are optimally

focused, can be calculated using the following formula involving beamformed PA signals using various scanlines and sound speeds,

$$Q(x; c) = \frac{1}{N} \sum_{z=1}^Z \sum_{n=1}^N |p_n(x, z; c) - \mu(x, z; c)|, \quad (2)$$

where X, Z is the number of scanlines and focal points per scanline in the ROI, N is the number of sensor elements, $p_n(x, z; c)$ is the focused PA signal with sound speed c for the z th focal point at the x th scanline, and $\mu(x, z; c)$ is the mean value of the focused PA signals $p_n(x, z; c)$.

In the mean sound speed estimation process, Q is first iteratively calculated for each scanline in the ROI using Eq. (2) while changing the sound speed. Then the scanline in the ROI providing the minimum Q value is determined as the center position of the absorber. Next, Q is iteratively calculated again for the scanline providing the minimum Q using various sound speeds. Finally, the sound speed providing the minimum Q value is selected to be the mean sound speed between the ROI and the sensor array.

2.3 Image reconstruction and evaluation

The estimated mean sound speed can then be used to reconstruct PA images by DAS, TR, UBP, and other reconstruction algorithms. We used the TR method in simulations because the setup sound speed distribution can be used to reconstruct exact PA images to evaluate the reconstructed PA image quality by using the estimated sound speed and any incorrect sound speed. On the other hand, because the sound speed distributions of phantoms are unknown and the proposed sound speed estimation method is based on optimal focusing, the DAS method was used to obtain the best performance. For comparison with the conventional method, the central vertical and lateral profiles of reconstructed absorbers are plotted. The relative amplitude, FWHM, and SNR are also measured to evaluate the performance of the proposed mean sound speed estimation method.

3. Numerical simulation

3.1 Homogeneous model

The simulation area is a 256×256 grid ($51.2 \times 51.2 \text{ mm}^2$), the number of sensor elements is 256, and the pitch of the sensor elements is 0.2 mm. The homogeneous model was set with a medium having a 1480 m/s sound speed with four pointlike absorbers placed at different depths and sensor positions under the sensor array as shown in Fig. 3(a). The propagation of optically excited PA signals was simulated by a k-wave MATLAB toolbox.³¹⁾ The

simulated PA signals are shown in Fig. 3(b). Gaussian noise of -20 dB was added to the simulated PA signals. Then the simulated PA signals were beamformed with various sound speeds. The beamformed PA signals with the correct sound speed of 1480 m/s for all four absorbers are shown in Fig. 4(a). As shown in the figure, the beamformed PA signal for absorber B is flat when optimally focused with the correct sound speed, scanline, and focal depth. Otherwise, the beamformed PA signal for absorber B is curved, as shown in Fig. 4(b), which was beamformed with the incorrect sound speed of 1700 m/s and the correct scanline, and focal depth for absorber B.

Then the focus quality value Q was calculated by averaging the sum of the deviations of the beamformed PA signals from their mean value, and is shown in Fig. 5(a) for each scanline in each ROI and in Fig. 5(b) for each sound speed at the scanline, which provides the minimum Q shown in Fig. 5(a). These figures show that the minimum Q is achieved at the scanline, which is the position of the absorber, and the minimum Q is also achieved at 1480 m/s for all ROIs, which is the specified sound speed in the homogeneous model. Figures 6(a) – 6(c) show TR-reconstructed PA images with the estimated mean sound speed of 1480 m/s, an arbitrary incorrect sound speed of 1400 m/s, and a generally used reconstruction sound speed of 1540 m/s, respectively.

The center-position lateral and vertical profiles of reconstructed absorber B are plotted in Figs. 7(a) and 7(b), respectively. The lateral FWHM of reconstructed absorber B is 0.8 mm for the estimated sound speed of 1480 m/s, 1.3 mm for 1540 m/s, and 1.6 mm for 1400 m/s. The vertical FWHM is 0.6 mm for 1480 m/s, 0.7 mm for 1540 m/s, and 0.7 mm for 1400 m/s. These results indicate that the intensity and spatial resolution of the reconstructed PA absorbers are improved. The SNR of reconstructed PA images can be calculated as

$$SNR = 10 \log_{10} \frac{S}{N} = 10 \log_{10} \frac{S_{peak}^2}{\sigma_{background}^2} = 10 \log_{10} \frac{\{\max[s(i, j)]\}^2}{\frac{1}{M \times N} \sum_{i=1}^M \sum_{j=1}^N \{s(i, j) - \mu_s\}^2}, \quad (3)$$

where S_{peak} is the maximum value of the image, $\sigma_{background}$ is the variance of the background, and the image size is $M \times N$. The calculated SNR is 58 dB for the estimated sound speed of 1480 m/s, 52 dB for the commonly used reconstruction sound speed of 1540 m/s, and 49 dB for the incorrect sound speed of 1400 m/s. This result indicates that the SNR of the reconstructed PA images was also improved.

3.2 Heterogeneous model

The heterogeneous model was set with four circular absorbers of 2 mm diameter placed at different depths and sensor positions under the sensor array shown in Fig. 8(a) and the heterogeneous sound speed distribution as shown in Fig. 8(b). The sound speed for the aqua blue area was set to 1450 m/s as the sound speed of porcine fat, which is lower than 1740 m/s selected for the sound speed of porcine red meat in the surrounding area.³²⁾

Figure 9(a) depicts the calculated focus quality value Q for each scanline in each ROI. The minimum Q is achieved at the sensor position that is the center position of the circular absorber. Figure 9(b) depicts the calculated focus quality value Q from 1440 to 1740 m/s with 20 m/s intervals. The minimum Q is achieved at 1580 m/s for ROIs A and C, 1560 m/s for ROI B, and 1540 m/s for ROI D. This result indicates that each estimated sound speed is the mean value between the ROI and the sensor array. The mean sound speeds of ROIs A and C were more affected by the sound speed of porcine red meat than that of porcine fat due to their greater depths in the porcine red meat than those of the ROIs B and D.

TR-reconstructed PA images using the exact sound speed distribution, the estimated sound speed of 1580 m/s for ROI C, and that of 1540 m/s for ROI D are presented in Fig. 10. The central lateral and vertical profiles of reconstructed absorber C are presented in Fig. 11. The lateral FWHM of reconstructed absorber C is 1.7 mm for the exact sound speed distribution, 1.8 mm for the estimated sound speed of 1580 m/s for ROI C, and 2.2 mm for the estimated sound speed of 1540 m/s for ROI D. The vertical FWHM is 1.8 mm for the exact sound speed distribution, 1.6 mm for 1580 m/s, and 1.5 mm for 1540 m/s. These results indicate that the proposed method can provide higher contrast and lateral spatial resolution than those of PA images reconstructed with other sound speeds and similar results to those of PA images reconstructed with exact sound speed distribution. The calculated SNR of the TR-reconstructed PA images is 35.5 dB for the estimated sound speed of 1580 m/s for ROI C, and 35.2 dB for the estimated sound speed of 1540 m/s for ROI D, which are in the same range but lower than the SNR for the exact sound speed distribution of 37.6 dB.

4. Phantom experiment

4.1 Experimental setup

The performance of the proposed method was also evaluated by agar and porcine tissue-mimicking phantoms with embedded thin and thick pencil lead absorbers. The system configuration is shown in Fig. 12. The output of an 800 nm optical parametric oscillation (OPO) laser (EKSPLA PG152B-T) pumped by a Q-switched Nd:YAG laser

(EKSPLA NL313G-30-SH-T) is injected into an optical fiber plated on both sides of a 7.5 MHz and 256-channel linear commercial US probe (Super Sonic Imagine SL15-4). The US system and laser system are synchronized with a function generator (Tektronix AFG3102C). The pulse repetition frequency (PRF) of the laser system is 30 Hz and the sampling rate of the data acquisition system is 30 MHz. The data acquisition time is about 33 s and 128-times signal averaging was achieved. Both RF and IQ data of the PA signals excited by the laser and the US signals excited by plane acoustic waves were acquired. Finally, mean sound speeds for each embedded absorber in all four ROIs were estimated to reconstruct PA images by using the DAS reconstruction algorithm.

4.2 Agar phantom

Four thin pencil lead absorbers of 0.5 mm diameter are embedded in a 50 (H) \times 50 (W) \times 60 (D) mm³ 1% agar phantom at different depths and sensor positions (Fig. 12). A US B-mode image obtained from the IQ data is shown in Fig. 13. From Fig. 13, we can confirm the presence of four embedded pencil leads.

The focus quality value Q for various scanlines and sound speeds is plotted in Figs. 14(a) and 14(b), respectively. As shown in Fig. 14(b), the minimum Q is found at a sound speed of 1480 m/s for all pencil leads, which is close to the mean sound speed of 1474 m/s of the agar phantom measured by the pulse-echo ultrasound method.³³⁻³⁴⁾

From the DAS-reconstructed PA images with an estimated mean sound speed of 1480 m/s [Fig. 15(a)], an arbitrary incorrect sound speed of 1400 m/s [Fig. 15(b)], and a generally used reconstruction sound speed of 1540 m/s [Fig. 15(c)], we can see that the contrast and spatial resolution of the reconstructed PA image with the estimated mean sound speed are higher than those of the reconstructed images with other sound speeds. The lateral and vertical profiles of reconstructed pencil lead B are presented in Fig. 16, from which we can also confirm the conclusion described above.

4.3 Porcine phantom

Four thick pencil lead absorbers of 2 mm diameter are embedded in a 30 (H) \times 50 (W) \times 40 (D) mm³ porcine phantom at different depths and sensor positions. The porcine phantom was immersed in 21.4 °C pure water and the probe was positioned 10 mm away from the top of the phantom. A schematic diagram and side view of the porcine phantom are shown in Fig. 17(a). The US B-mode image obtained from the IQ data is shown in Fig. 17(b). Only the top two leads, leads C and D, can be confirmed due to the high attenuation

of acoustic waves.

The focus quality values Q for different scanlines and sound speeds are plotted in Figs. 18(a) and 18(b), respectively. As shown in Fig. 18(b), the minimum Q is found at 1580 m/s for ROI C and 1540 m/s for ROI D, which are close to the results of the simulation. The mean sound speed of ROI C is larger than that of ROI D because pencil lead C is placed deeper in the porcine red meat than pencil lead D, and both estimated sound speeds are close to the mean sound speeds between the ROIs and the sensor array. The mean sound speeds for ROIs A and B cannot be estimated because of the low PA signal level due to the high attenuation and scattering of acoustic waves and laser energy. The depth and off-center position of the absorber can also reduce the intensity of PA signals significantly. All these factors result in the invisibility of leads A and B in DAS-reconstructed PA images as shown in Fig. 19.

5. Discussion

There are several issues to be discussed further. In this study, we calculated the focus quality value Q for each scanline in the ROIs to estimate the optimum mean sound speed between the ROI and the sensor array. Thus, the proposed method is broadly applicable to both pointlike absorbers and large-diameter absorbers as shown in the simulations and experiments. Therefore, the proposed method is more widely applicable than estimating the mean sound speed by calculating the coherence factor (CF) of beamformed PA signals, which is usually useful for only pointlike absorbers.³⁵⁾ Mean sound speed estimation using focusing compensation is usually inapplicable for long-line absorbers (for example, blood vessels), because the wavefront of PA signals excited by a long-line absorber is almost flat. In order to discuss the limitation of the detectable width of the line absorber, we simulated five 0.6-mm-diameter point-line absorbers located at the same depth with the distance between the absorbers changed from 0 to 0.4 mm at 0.2 mm increments in the homogeneous model. Note that the distances between the small absorbers are less than their diameter. Thus we can consider all five small absorbers as one line absorber (distance = 0 mm) or one large-width absorber (distance = 0.2, 0.4 mm). A close-up of the ROI in the simulation model and the calculated focus quality value Q curve for each sound speed are shown in Figs. 20(a) and 20(b), respectively. Figure 20(b) indicates that the mean sound speed can be estimated even with multiple absorbers at the same depth in one ROI but the distance between the absorbers must be smaller than approximately 0.4 mm because the calculated Q curve rapidly becomes flat with increasing distance. In this case, from Fig.

20(a), we know that the width of all five absorbers is 4.6 mm. In other words, the detectable width for the large absorber in the ROI is up to approximately 4.6 mm.

In addition, the proposed method is robust against noise because PA signals are usually induced by a strong optical absorber and the amplitude is generally higher than the noise level. In addition to noise, another two factors can affect the accuracy of the proposed method. The amplitude of PA signals can be reduced significantly due to strong optical attenuation, absorption, and scattering of medium even with a strong absorber shown in the porcine phantom.³⁶⁾ Also, sidelobes from strong absorbers outside the ROI may affect the accuracy of sound speed estimation when the ROI contains only weak absorbers,³⁷⁾ because all the sensor data is used to calculate the focus quality value. This limitation can be improved by using only sensor data in the ROI or by implementing an apodization filter.

The proposed method is implemented in MATLAB (MathWorks R2014a) on a workstation having one core i5 2.60 GHz CPU and 4 GB RAM (DELL Latitude E6230). The computation time of the proposed method is determined by the size of the ROI and the number of swept sound speeds. In the phantom experiments, the ROI contained 31 scanlines and 201 focus points (approx. $9 \times 9 \text{ mm}^2$) and the number of swept sound speeds was 15. Under these conditions, the computation time is approximately 314. The computation time can be reduced by using a small ROI and fewer sound speeds, which may bring errors in accuracy, or by implementing a program with parallel computation, or by using a standard optimization method.³⁸⁾ The reconstructed images using the DAS and TR reconstruction algorithms with the estimated mean sound speed can provide better image quality as shown in the simulations and experiments. We should note that the estimated sound speed is the mean value between the ROI and the sensor array and that it provides higher image quality than that of reconstruction without sound speed estimation. Although the proposed method can output better reconstructed images, artifacts such as sidelobes are still distinct. In future works, we will improve the accuracy of sound speed estimation and continuously verify the usability for the UBP reconstruction algorithm. As a next step, we would like to develop another focus quality evaluation approach that can be flexibly adapted to more complicated situations, such as blood vessels.

6. Conclusion

In this study, we have estimated the mean sound speed by calculating the minimum average sum of the difference of beamformed PA signals from their mean value. The proposed method was verified by numerical simulations and tissue-mimicking phantom experiments.

The images reconstructed using the estimated optimum mean sound speed provide higher contrast and SNR and better spatial resolution.

Acknowledgment

This study was supported in part by a grant of the Strategic Research Foundation Grant-aided Project for Private Universities by the Ministry of Education, Culture, Sports, Science and Technology, Japan (MEXT), S1311037.

References

- 1) M. H. Xu and L. V. Wang, *Rev. Sci. Instrum.* **77**, 041101 (2006).
- 2) L. V. Wang and L. Gao, *Annu. Rev. Biomed. Eng.* **16**, 155 (2014).
- 3) S. Manohar, S. E. Vaartjes, J. C. G. Hespen, J. M. Klaase, F. M. Engh, W. Steenbergen, and T. G. Leeuwen, *Opt. Express* **15**, 12277 (2007).
- 4) H. F. Zhang, K. Maslov, G. Stoica, and L. V. Wang, *Nat. Biotechnol.* **24**, 848 (2006).
- 5) M. L. Li, J. T. Oh, X. Y. Xie, G. Ku, W. Wang, C. Li, G. Lungu, G. Stoica, and L. V. Wang, *Proc. IEEE* **96**, 481 (2008).
- 6) J. Laufer, C. Elwell, D. Delpy, and P. Beard, *Phys. Med. Biol.* **50**, 4409 (2005).
- 7) E. Z. Zhang, J. G. Laufer, R. B. Pedley, and P. C. Beard, *Phys. Med. Biol.* **54**, 1035 (2009).
- 8) E. Zhang, J. Laufer, and P. Beard, *Appl. Opt.* **47**, 561 (2008).
- 9) B. Cong, K. Kondo, M. Yamakawa, T. Shiina, T. Nakajima, and Y. Asao, *IEEJ Trans. Electr. Electron. Eng.* **9**, 477 (2014).
- 10) S. Mallidi, G. P. Luke, and S. Emelianov, *Trends Biotechnol.* **29**, 213 (2011).
- 11) S. Kim, Y. S. Chen, G. P. Luke, M. Mehrmohammadi, J. R. Cook, and S. Y. Emelianov, *Proc. IEEE Ultrasonics Symp.*, 2010, p. 233.
- 12) E. Z. Zhang, J. Laufer, B. Povazay, A. Alex, B. Hofer, W. Drexler, and P. Beard, *Proc. SPIE* **7564**, 75640U (2010).
- 13) C. G. A. Hoelen and F. M. Mul, *Appl. Opt.* **39**, 5872 (2000).
- 14) M. Xu and L. V. Wang, *Phys. Rev. E* **71**, 016706 (2005).
- 15) M. Xu and L. V. Wang, *IEEE Trans. Med. Imaging* **21**, 814 (2002).
- 16) M. Xu and L. V. Wang, *Phys. Rev. E* **67**, 056605 (2003).
- 17) P. Burgholzer, G. J. Matt, M. Haltmeier, and G. Paltauf, *Phys. Rev. E* **75**, 046706 (2007).
- 18) Y. Xu and L. V. Wang, *Phys. Rev. Lett.* **92**, 033902 (2004).
- 19) G. Paltauf, J. A. Viator, S. A. Prahl, and S. L. Jacques, *J. Acoust. Soc. Am.* **112**, 1536 (2002).
- 20) S. Ma, S. Yang, and H. Guo, *J. Appl. Phys.* **106**, 123104 (2009).
- 21) S. Bu, Z. Liu, T. Shiina, K. Kondo, M. Yamakawa, K. Fukutani, Y. Someda, and Y. Asao, *IEEE Trans. Biomed. Eng.* **59**, 1354 (2012).
- 22) Y. Hristova, P. Kuchment, and L. Nguyen, *Inverse Probl.* **24**, 055006 (2008).
- 23) B. T. Cox and B. E. Treeby, *IEEE Trans. Med. Imaging* **29**, 387 (2010).
- 24) M. E. Anderson, M. S. McKeag, and G. E. Trahey, *J. Acoust. Soc. Am.* **107**, 3540 (2000).
- 25) J. Qian, P. Stefanov, G. Uhlmann, and H. Zhao, *J. Imaging Sci.* **4**, 850 (2011).

- 26) X. Jin and L. V. Wang, *Phys. Med. Biol.* **51**, 6437 (2006).
- 27) B. E. Treeby, T. K. Varshney, E. Z. Zhang, J. G. Laufer, and P. C. Beard, *J. Biomed. Opt.* **16**, 090501 (2011).
- 28) D. Napolitano, C. H. Chou, G. McLaughlin, T. L. Ji, L. Mo, D. DeBusschere, and R. Steins, *Ultrasonics* **44**, e43 (2006).
- 29) C. Yoon, Y. Lee, J. H. Chang, T. Song, and Y. Yoo, *Ultrasonics* **51**, 795 (2011).
- 30) J. A. Jensen and P. Munk, *Acoust. Imaging* **23**, 75 (1997).
- 31) B. E. Treeby and B. T. Cox, *J. Biomed. Opt.* **15**, 021314 (2010).
- 32) K. Miyazawa, K. Kanno, and M. Tabata, *J. Swine Res.* **14**, 63 (1977).
- 33) M. E. Anderson and G. E. Trahey, *J. Acoust. Soc. Am.* **104**, 3099 (1998).
- 34) V. A. D. Grosso and C. W. Mader, *J. Acoust. Soc. Am.* **52**, 1442 (1972).
- 35) C. Yoon, J. Kang, S. Han, Y. Yoo, T. Song, and J. H. Chang, *Opt. Express* **20**, 3082 (2012).
- 36) L. Wang, S. L. Jacques and L. Zheng, *Comput. Methods Programs Biomed.* **47**, 131 (1995).
- 37) C. C. Nilsen and S. Holm, *IEEE Trans. Ultrason. Ferroelectr. Freq. Control* **57**, 1329 (2010).
- 38) J. Fu, L. Lei, and G. Zhou, *Proc. Int. Workshop Adv. Comput. Intelligence*, 2010, p. 260.

Figure Captions

Fig. 1. (Color online) Detected PA signals (a) from a pointlike optical absorber by a 32-channel linear sensor array (b).

Fig. 2. (Color online) Focused PA signals using the real sound speed (a) and summed signals of focused (b) and defocused (c) PA signals.

Fig. 3. (Color online) Homogeneous sound speed simulation model (a) and simulated PA signals with -20 dB Gaussian noise (b).

Fig. 4. (Color online) Focused PA signals with the setup sound speed of 1480 m/s (a) and defocused PA signals with an arbitrary incorrect sound speed of 1700 m/s (b) for absorber B in homogeneous model.

Fig. 5. (Color online) Calculated focus quality value Q for each scanline in each ROI (a) and for various sound speeds at each scanline providing the minimum Q value (b).

Fig. 6. (Color) TR-reconstructed PA images with estimated mean sound speed of 1480 m/s (a), incorrect sound speed of 1400 m/s (b), and generally used reconstruction sound speed of 1540 m/s (c).

Fig. 7. (Color online) Lateral (a) and vertical (b) profiles of reconstructed absorber B.

Fig. 8. (Color online) Sound speed distribution (a) and configuration diagram (b) of heterogeneous simulation model.

Fig. 9. (Color online) Calculated focus quality value Q for various scanlines (a) and various sound speeds (b).

Fig. 10. (Color) TR-reconstructed images with exact sound speed distribution (a), estimated sound speed of 1580 m/s for ROI C (b), and estimated sound speed of 1540 m/s for ROI D (c).

Fig. 11. (Color online) Central lateral (a) and vertical (b) profiles of reconstructed circular absorber C shown in Fig. 10.

Fig. 12. (Color online) System configuration for phantom experiments.

Fig. 13. (Color online) US B-mode image obtained from received IQ data.

Fig. 14. (Color online) Calculated focus quality value Q for various scanlines (a) and sound speeds (b) for pencil leads A – D.

Fig. 15. (Color) DAS-reconstructed images with estimated mean sound speed 1480 m/s (a) and other incorrect sound speeds (b), (c).

Fig. 16. (Color online) Lateral (a) and vertical (b) profiles of reconstructed thin pencil lead B shown in Fig. 15.

Fig. 17. (Color online) Schematic diagram and side view of porcine phantom (a) and US B-mode image obtained from received IQ data (b).

Fig. 18. (Color online) Calculated focus quality value Q for different scanlines (a) and sound speeds (b) for ROIs A – D.

Fig. 19. (Color) DAS-reconstructed images with estimated sound speeds of 1540 m/s for ROI D (a), 1580 m/s for ROI C (b), and arbitrary incorrect sound speed of 1500 m/s (c).

Fig. 20. (Color online) Simulation model with five 0.6-mm-diameter absorbers in one ROI with distance between absorbers changed from 0 to 0.4 mm (a) and calculated Q curve for each sound speed (b).

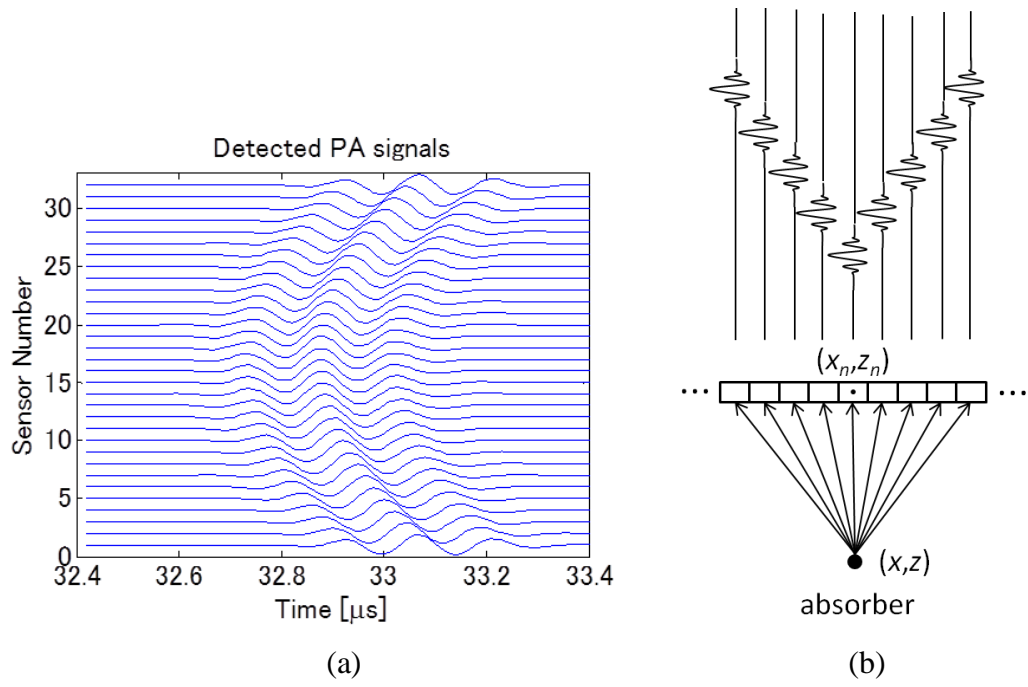


Fig. 1. (Color Online)

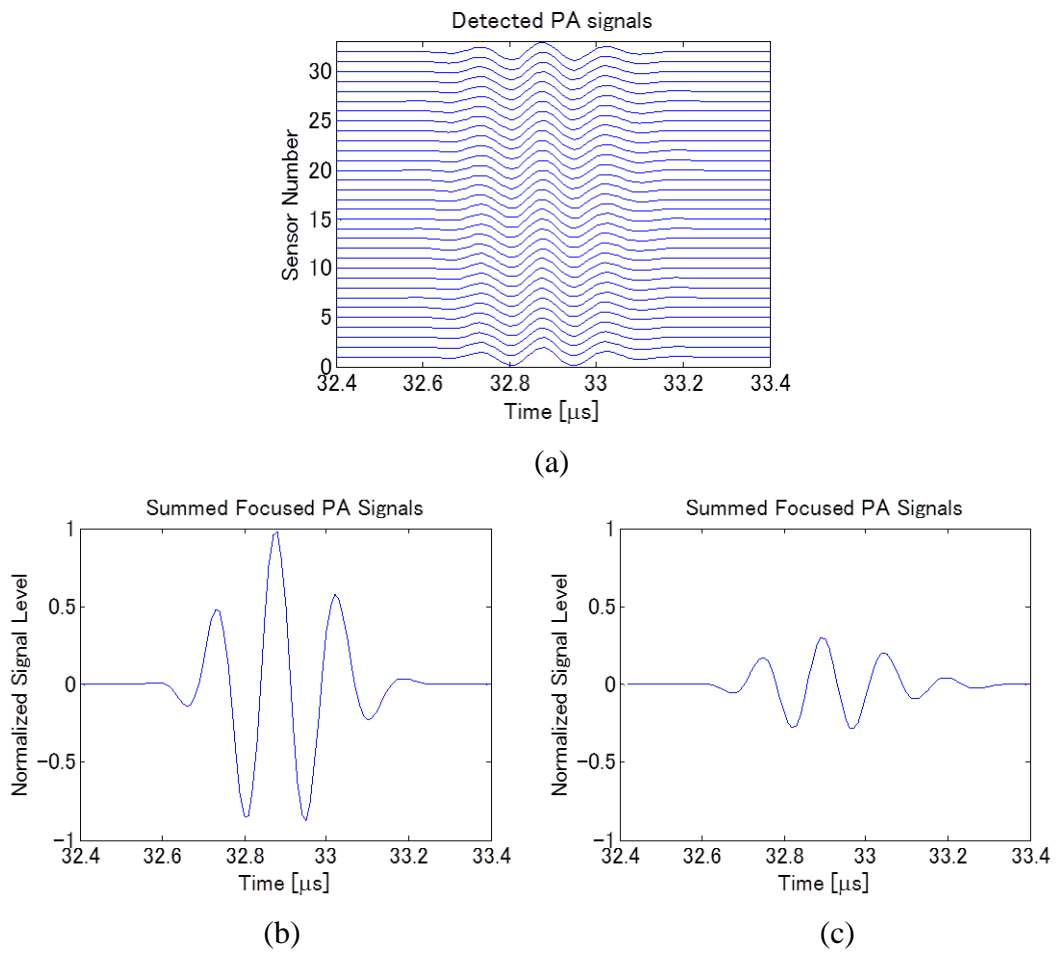
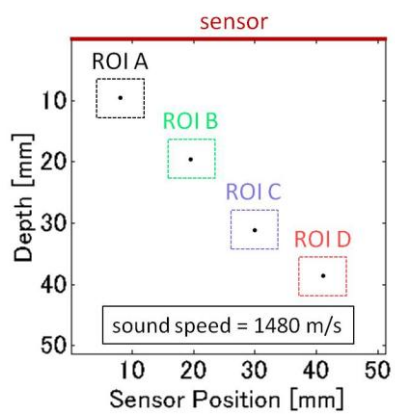
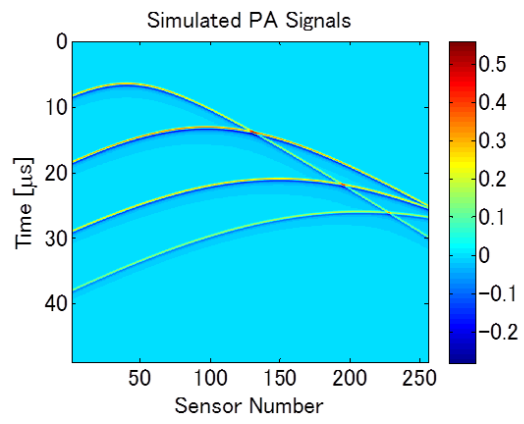


Fig. 2. (Color Online)

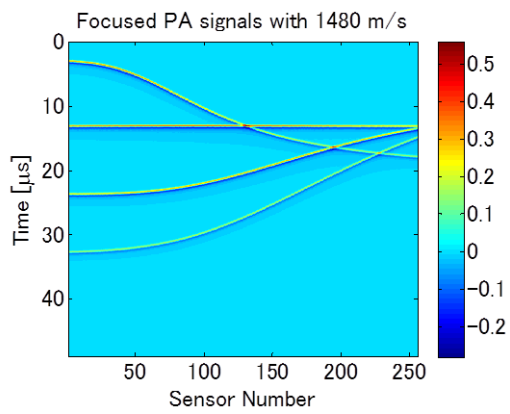


(a)

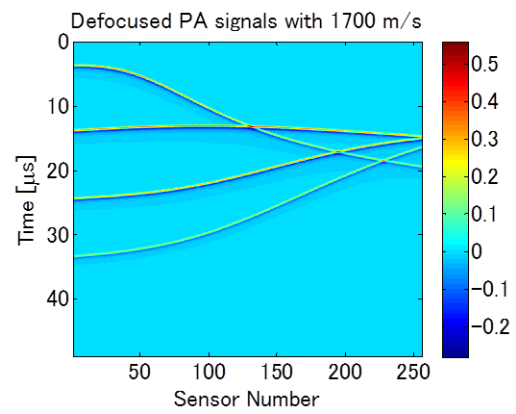


(b)

Fig. 3. (Color Online)



(a)



(b)

Fig. 4. (Color Online)

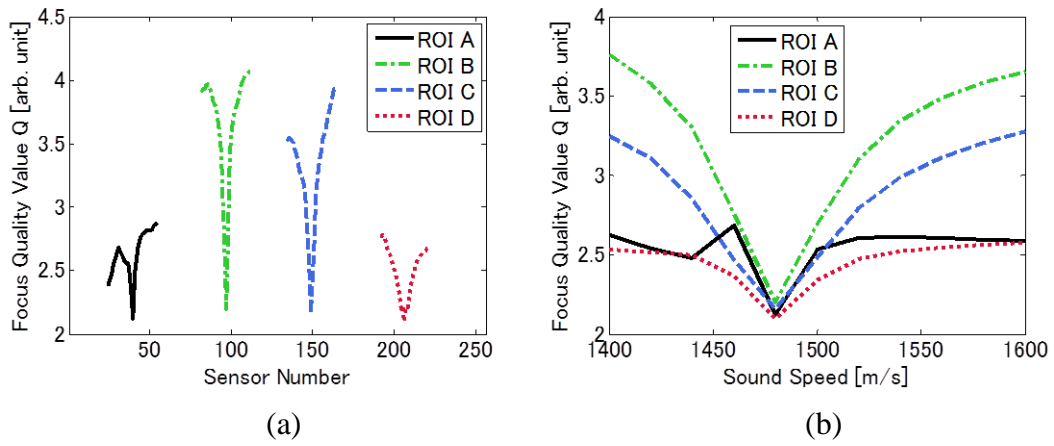


Fig. 5. (Color Online)

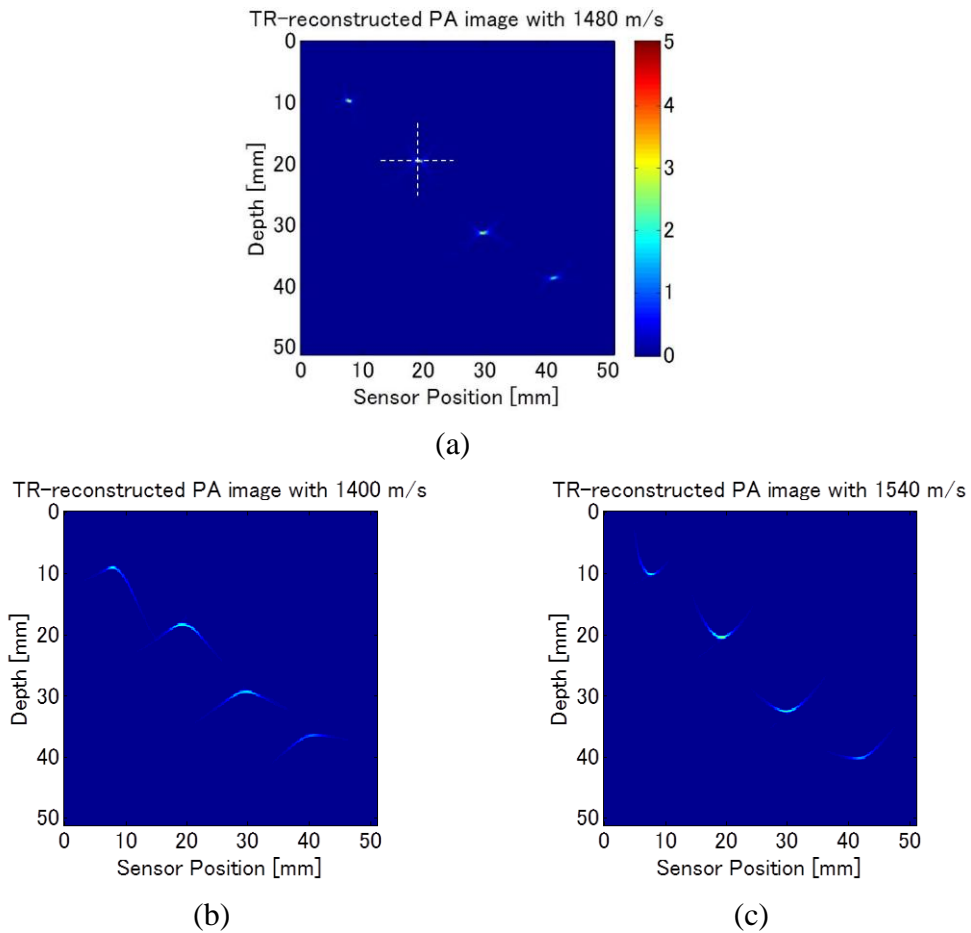


Fig. 6. (Color)

Color Print

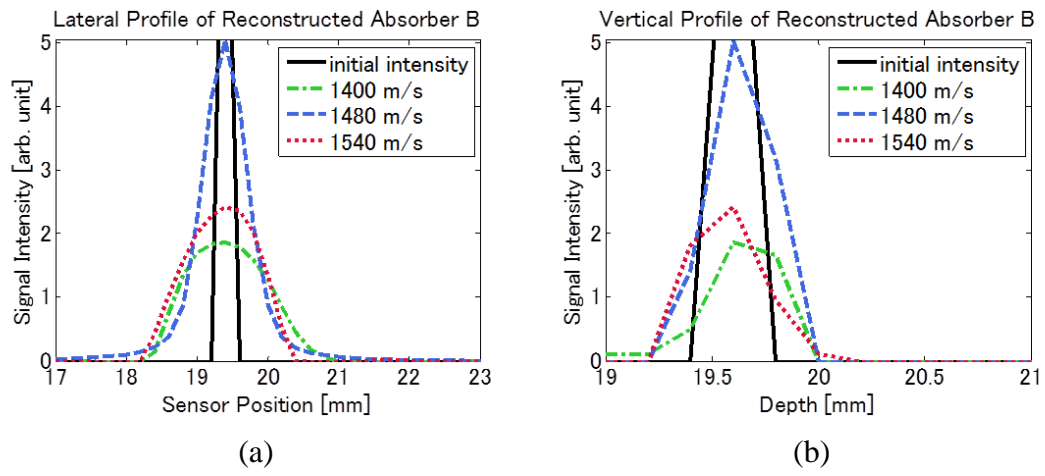


Fig. 7. (Color Online)

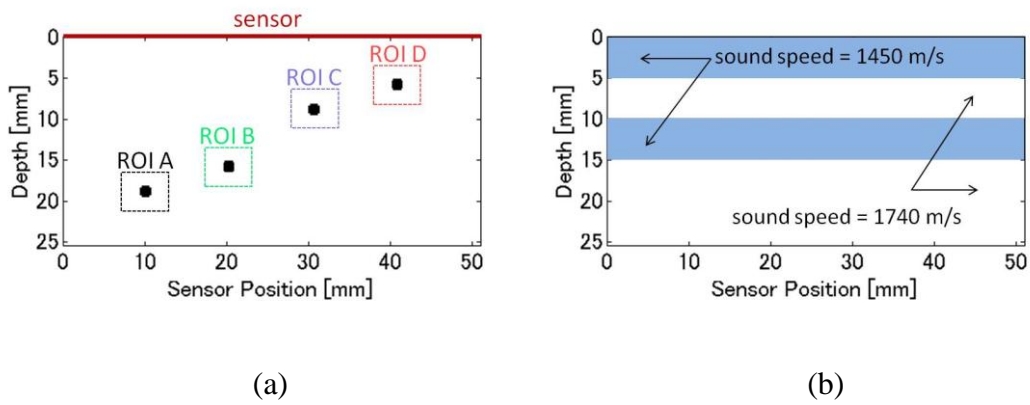


Fig. 8. (Color Online)

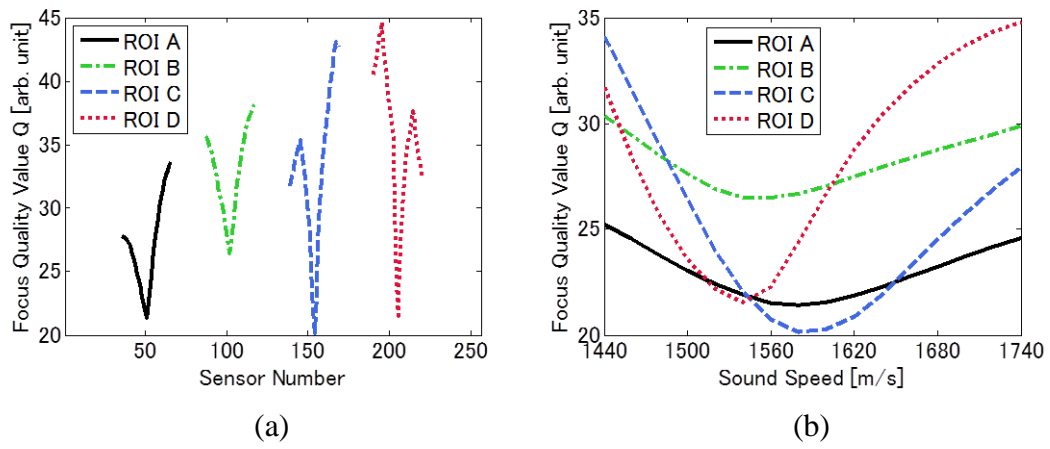


Fig. 9. (Color Online)

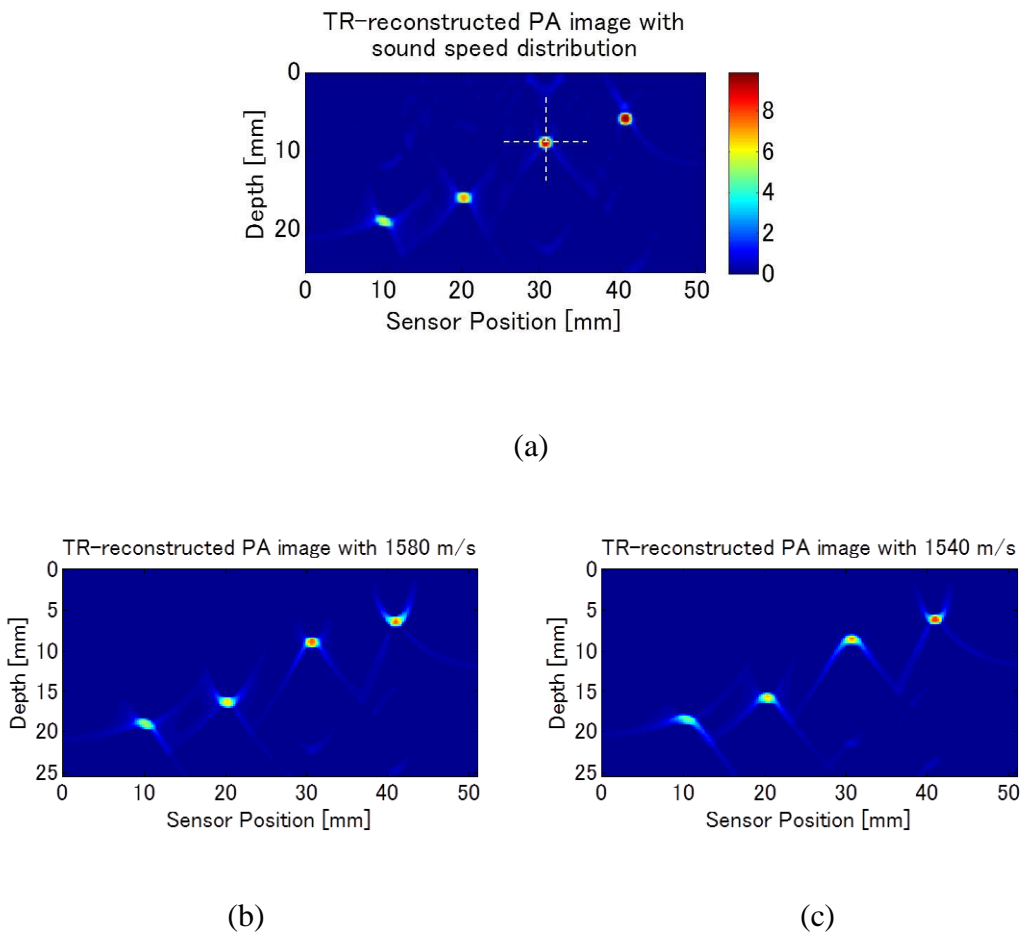


Fig. 10. (Color)

Color Print

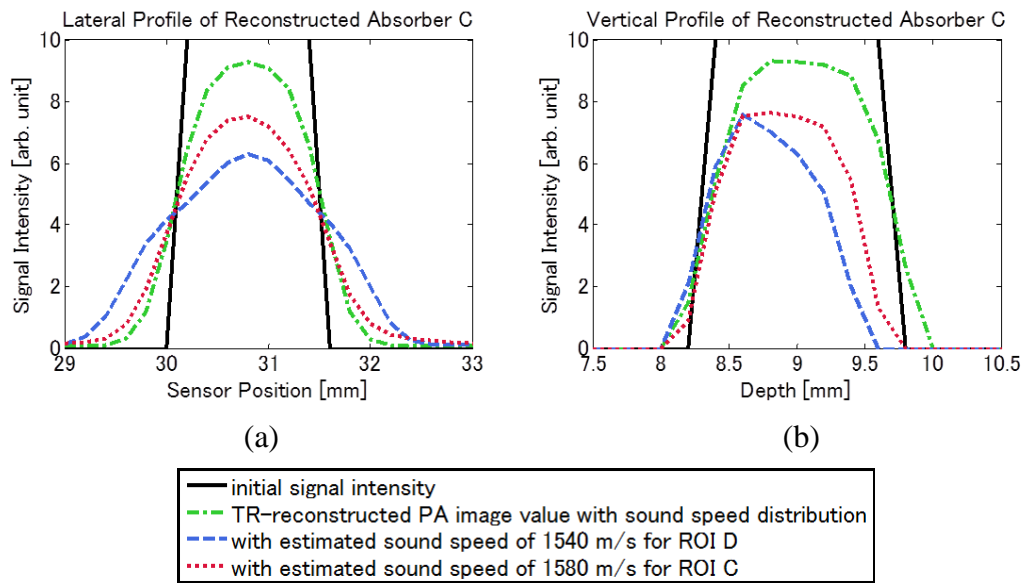


Fig. 11. (Color Online)

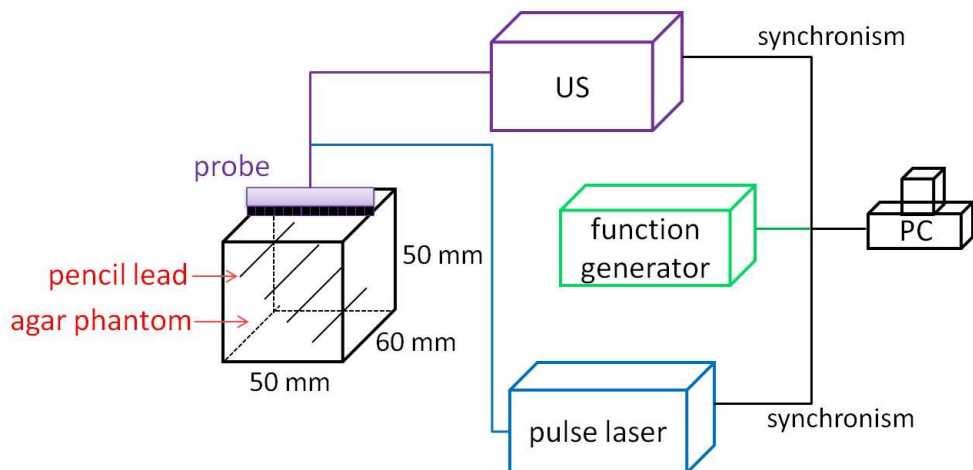


Fig. 12. (Color Online)

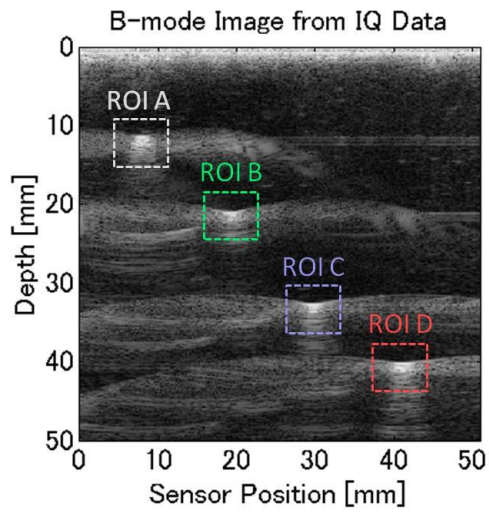


Fig. 13. (Color Online)

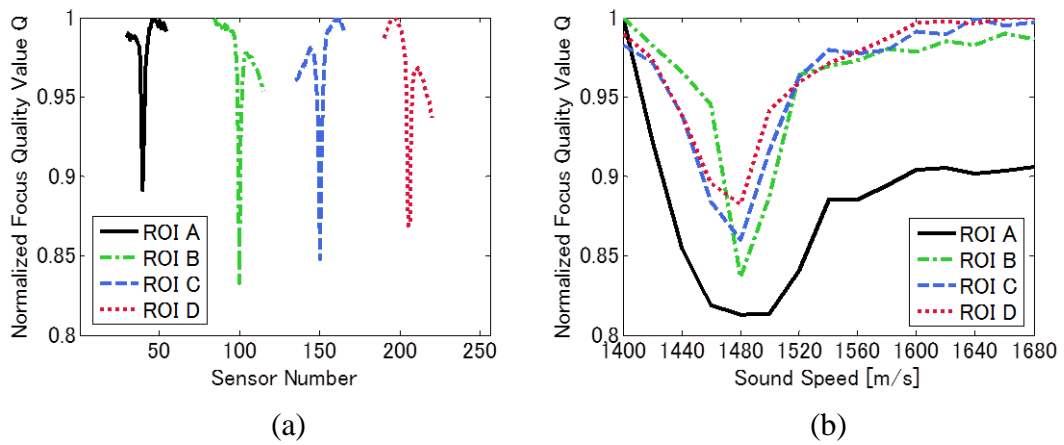
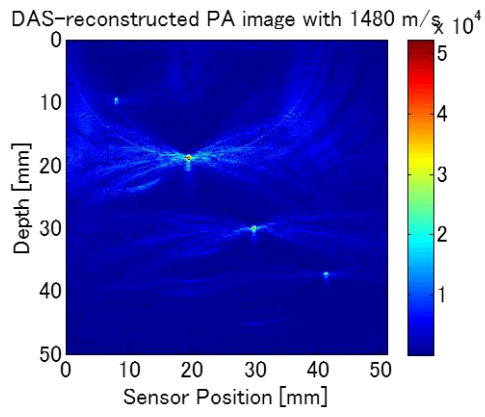
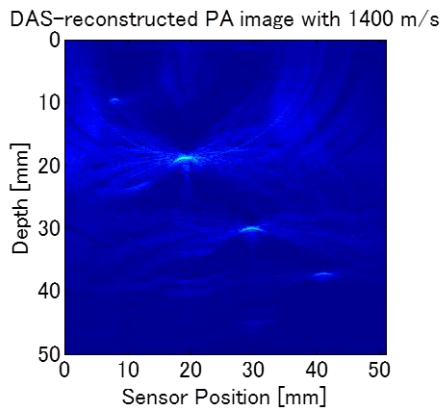


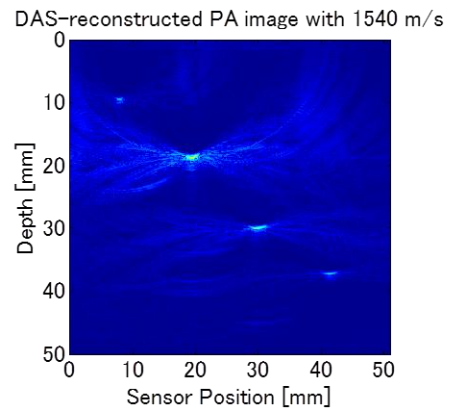
Fig. 14. (Color Online)



(a)



(b)



(c)

Fig. 15. (Color)

Color Print

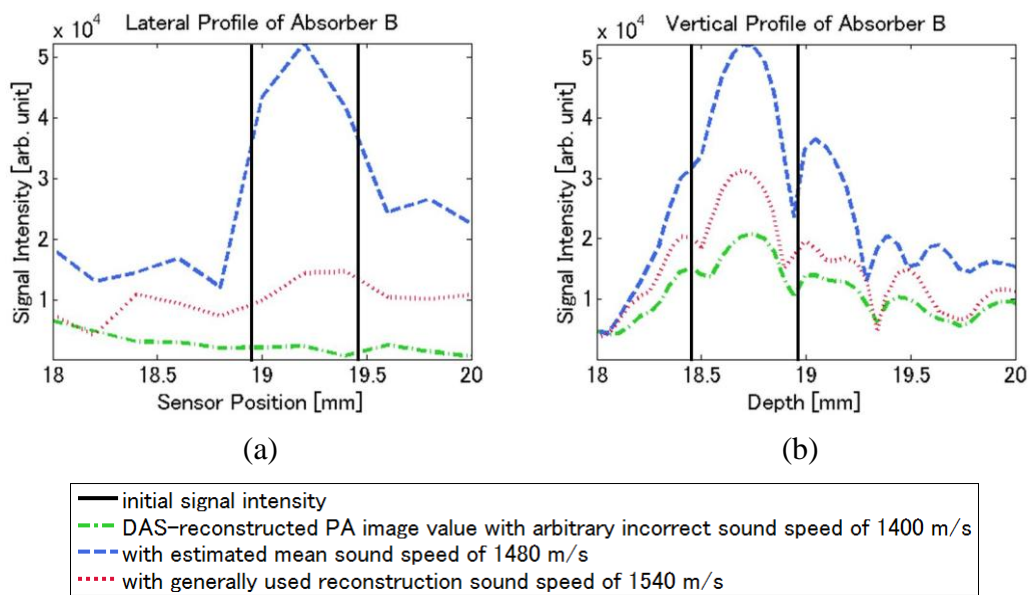


Fig. 16. (Color Online)

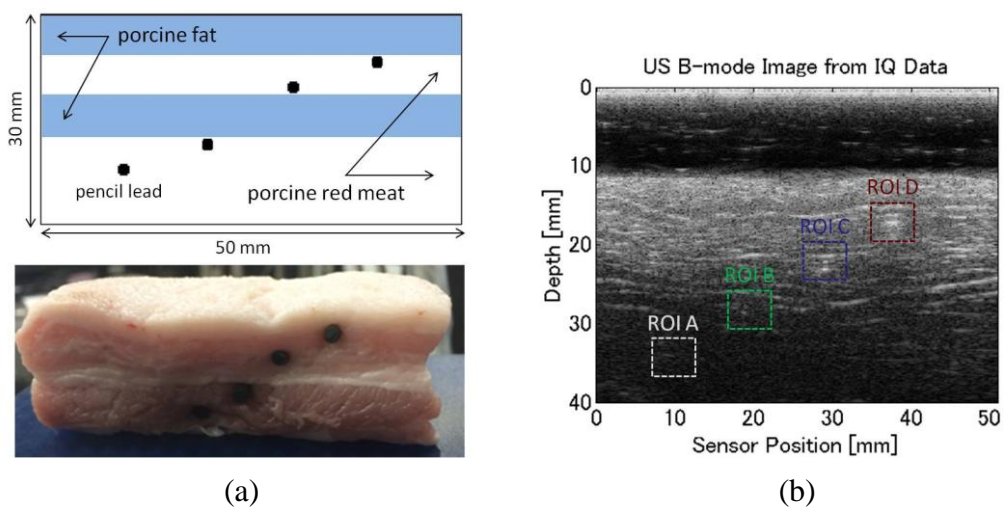


Fig. 17. (Color Online)

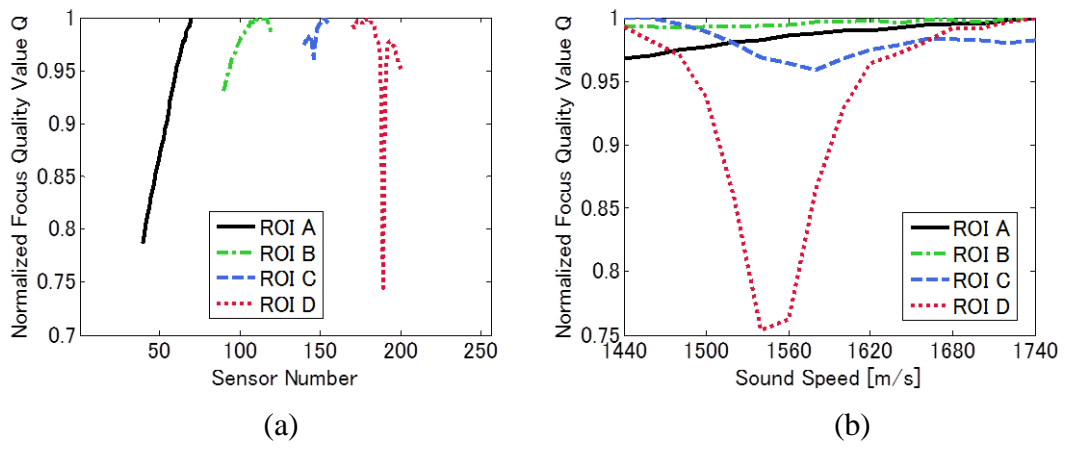


Fig. 18. (Color Online)

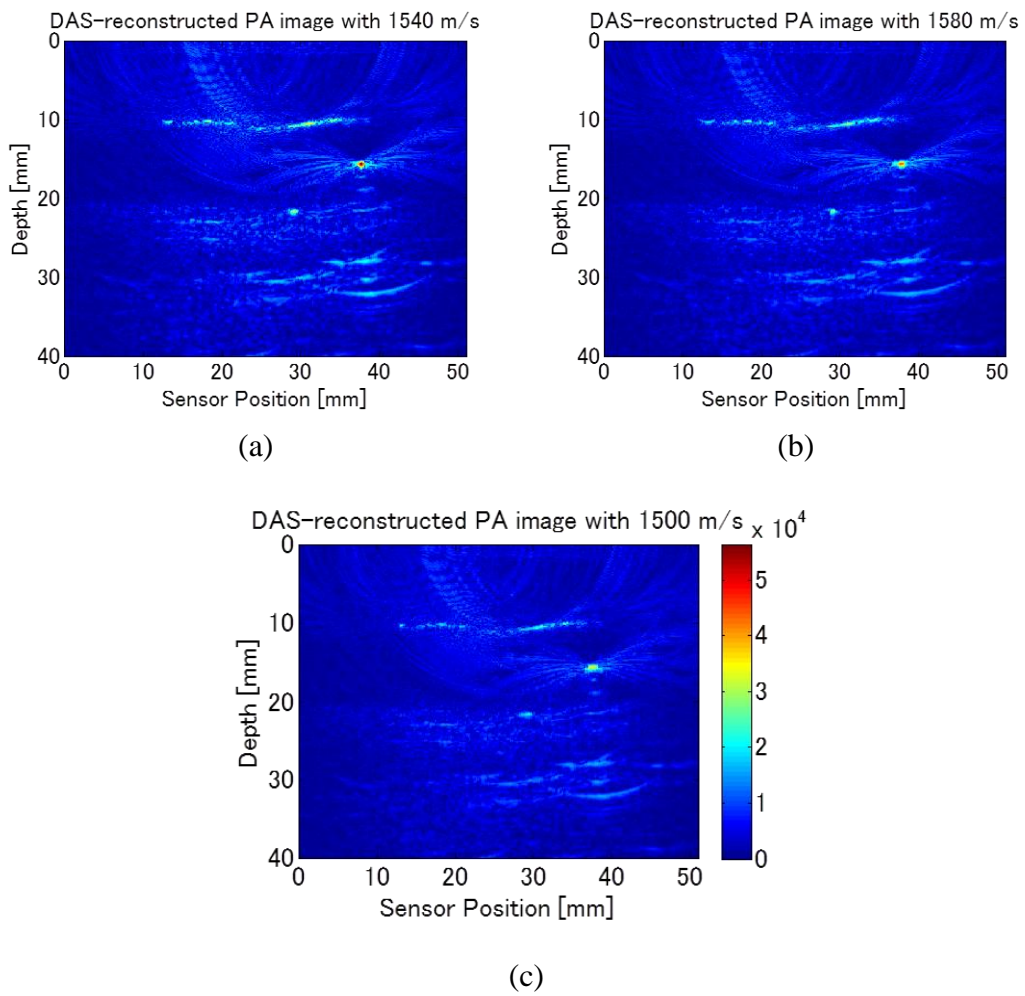


Fig. 19. (Color)

Color Print

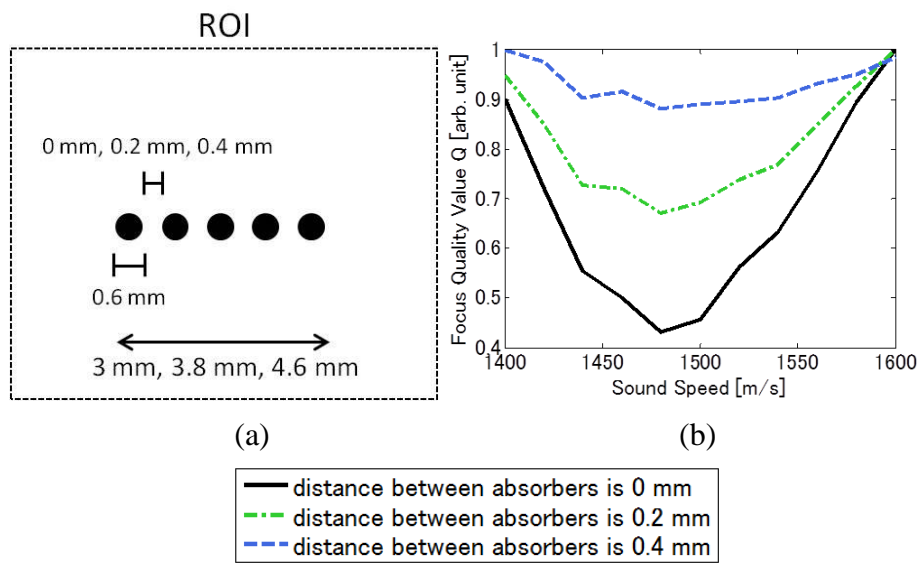


Fig. 20. (Color Online)